NOVA SCHOOL OF SCIENCE & TECHNOLOGY

DEPARTMENTS OF:
Physics
Materials
Life Sciences
Chemistry

Rui Pedro Santos Silva

BSc in Biochemistry

Assessing the Effects of Scaffold Porosity and Geometry on Mechanical Properties and Cell Alignment

MASTER IN BIOMATERIALS AND NANOMEDICINE

NOVA University Lisbon
September, 2024

NOVA SCHOOL OF SCIENCE & TECHNOLOGY

DEPARTMENTS OF:

Physics

Materials

Life Sciences

Chemistry

Assessing the Effects of Scaffold Porosity and Geometry on Mechanical Properties and Cell Alignment

Rui Pedro Santos Silva

BSc in Biochemistry

Adviser: Henrique Vazão de Almeida
Researcher, CENIMAT|i3N NOVA University Lisbon
Miguel Dias Castilho
Assistant Professor, BDP Eindhoven University of Technology

Co-advisers: Gerardo Cedillo Servin
PhD candidate, *Eindhoven University of Technology*

Examination Committee:

Chair: Dr. Luís Alexandre Almeida Fernandes,
Full Professor, FCT-NOVA

Rapporteurs: João Carlos Fernandes da Silva,
Researcher at Institute for Bioengineering and Biosciences (iBB), IST

Adviser: Henrique Vazão de Almeida,
Researcher, CENIMAT|i3N NOVA University Lisbon

Members: Miguel Dias Castilho,
Assistant Professor, Eindhoven University of Technology

MASTER IN BIOMATERIALS AND NANOMEDICINE
NOVA University Lisbon
September, 2024

Assessing the Effects of Scaffold Porosity and Geometry on Mechanical Properties and Cell Alignment

Rui Pedro Santos Silva

This work was conducted in collaboration with:

Eindhoven University of Technology | TU/e

Biomaterials Design & Processing Group

Supervised by:

Assistant Professor Miguel Dias Castilho

Eindhoven University of Technology
September, 2024

Assessing the Effects of Scaffold Porosity and Geometry on Mechanical Properties and Cell Alignment

This document was created with Microsoft Word text processor and the NOVA thesis Word template

ACKNOWLEDGMENTS

First of all, I'd like to thank my Professors, Henrique Almeida and Miguel Castilho, for their dedication throughout this academic year, for coming together to offer me one of the best experiences of my life, and above all, for their care and support for both me and my work during this time.

I would also like to give a special thanks to Gerardo for all the help and guidance he provided; without his dedication and willingness to teach, none of the work presented here would have been possible. I'd like to extend my thanks to Jirawat, Essa, Marcela, and Vasco, who were fantastic with me and always made time to help whenever I needed it. I'm also grateful to everyone at CENIMAT and TU/e who, directly or indirectly, contributed to making this project a reality.

To my parents and brother, I want to express my gratitude for all the support and love over these past five years and for giving me the opportunity to have this experience in Eindhoven. Likewise, I want to thank my grandparents for all their support and affection throughout the years. Lastly, to my cousins and uncles, thank you for all the support you've given me.

To the best Tu/e Researchers, Mariana, Diana, Linda, Tom.H, Yas ... I have to thank you for everything over the last year; being with you every day has really motivated me to do my best work. Tommy, a special thank you for being my daily partner and listening to all my dramas, thank you for our friendship. I wish you all the best and that we remain together.

Rosarinho, I have no words for you. You have been my biggest support and my best friend during this experience; all I wanted was one more day in Socialhub with you. João and Rodrigo, you're my two favorites; you've been great friends to me and I couldn't imagine a better friendship than the one you gave me. Thank you three for making me happy.

To the Social_buddies, Leo and Roksy, thank you for all the evenings, study sessions and birthdays that the three of us had to outdo (in nostalgia). Our stay in this residence will never be forgotten by us or them. Until our next wine and cheese session. Also, to all my friends I made during my final year, Duarte, Ravi, Silvia, Fran, Mauro, Marijn, Tim, thank you for everything during this Erasmus experience.

For my enzyme who knows me better than I know myself, for my best friend who guides me in every decision in my life and for my best friend who I miss all the time. Dalila, Rita and Gon, this thesis is also dedicated to you who have walked alongside me since the beginning.

To my little ones, Inês, Oriana and Baptista, thank you for listening to me complain a thousand times meaninglessly and still prove me right, being proud of you makes me grow and made my entire academic life happier. To my Afonso, I thank you for the friendship and mutual affection we have, it makes me happy to see you grow and be able to support you in the best way I can, just as you do with me.

Finally, I dedicate this work to my childhood friends who have always supported me and were part of all my personal and academic choices, you are my calm and my breath. Lima, Goreti, Rita, Leonor, Beatriz and Patrícia you are home. To Tixa and Bia I leave a special note for having overcome this challenge together and that we can achieve all our goals.

“Life is a long fall […] The most important thing
is knowing how to fall.”

Joël Dicker

ABSTRACT

Ischemic heart disease and consequent myocardial infarction are a global health emergency. These conditions are responsible for permanent cell death and the formation of scar tissue. The lack of regenerative capacity of cardiac muscle cells associated with current therapeutic limitations, leads cardiac tissue engineering to develop new strategies in this area to mimic the microenvironment of myocardium . Cardiac cells are highly specialized, providing the heart muscle a mechanical and electrical behavior that is complex to replicate. The anisotropic nature and cell microenvironment become the greatest challenges in the production of materials capable of supporting cell growth and organization.

In this master thesis it was proposed the manufacture of three dimensional hexagonal polycaprolactone scaffolds using melt electrowriting, an additive manufacturing technique, design to mimic the mechanical parameters of the myocardium and its anisotropic composition. The scaffolds were manufactured with two pore sizes, where the hexagonal structures had different side length of 400 µm and 600 µm with different internal angles (30 °, 45 ° and 60 °). The scaffolds were incubated in Gelatin Methacryloyl hydrogel with human mesenchymal stem cells to study the alignment and orientation of the cells in the different geometries.

The melt electrowriting-fabricated scaffolds were subjected to uniaxial tensile tests where they showed an anisotropic mechanical behavior, a high strength and low stiffness; parameters that can be made more similar to native tissue by adding fibers to the structure. The cell patches were subjected to PrestoBlue assays to assess the viability over time, the cell metabolic activity showed to grow over time in all groups according to the positive control. Finally, cytoskeletal F-actin was labeled with phalloidin and observed by confocal microscopy, revealing a greater cell alignment in the scaffolds with lower internal angle of 30 °.

In addition to the proposed work, it was idealized to place conductive nanoparticles such as MXenes to the structures in order to increase cell synchronization and consequently maturation between them. For this, preliminary tests were initiated in order to understand which strategy ensures a uniform distribution of MXenes along the fibers.

Keywords: Anisotropy, Cardiomyocyte, Melt electrowriting, Myocardium, Scaffolds

RESUMO

A doença isquémica cardíaca e o consequente enfarte do miocárdio são uma emergência de saúde global. Estas condições são responsáveis pela morte celular permanente e pela formação de tecido cicatricial. A falta de capacidade regenerativa das células do músculo cardíaco, associada às limitações terapêuticas atuais, leva a engenharia do tecido cardíaco a desenvolver novas estratégias nesta área para simular o microambiente do miocárdio. As células cardíacas são altamente especializadas, proporcionando ao músculo cardíaco um comportamento mecânico e elétrico complexo de replicar. A natureza anisotrópica e o microambiente tornam-se os maiores desafios na produção de materiais capazes de suportar o crescimento e organização celular.

Nesta dissertação de mestrado propôs-se o fabrico de *scaffolds* de policaprolactona hexagonal 3D utilizando uma técnica de fabrico aditivo, o *melt electrowriting*, desenho para mimetizar os parâmetros mecânicos do miocárdio e a sua composição anisotrópica. Os *scaffolds* foram fabricados com dois tamanhos de poros, caracterizados por hexágonos com diferentes tamanho de lado, 400 µm and 600 µm, nos quais continham ângulos internos diferentes (30 °, 45 ° e 60 °) e, em seguida, foram incubados em hidrogel de *Gelatin Methacryloyl* com células estaminais do mesênquimahumanas para estudar o alinhamento e orientação das células nas diferentes geometrias.

Os *scaffolds* fabricados por *melt electrowriting* foram submetidos a ensaios de tração uniaxiais onde apresentaram comportamento mecânico anisotrópico, alta resistência e baixa rigidez; parâmetros que podem ser tornados mais semelhantes ao tecido nativo, adicionando fibras à estrutura. Os *cellular patches* foram submetidos a ensaios PrestoBlue para avaliar a viabilidade ao longo do tempo, a atividade metabólica celular mostrou crescer ao longo do tempo em todos os grupos de acordo com o controle positivo. Finalmente, a F-actina do citoesqueleto foi marcada com *phalloidin* e observada por microscopia confocal, revelando um maior alinhamento celular nos *scaffolds* com um ângulo interno de 30°.

Além do trabalho proposto, idealizou-se colocar nanopartículas condutoras, como MXenes, nas estruturas, a fim de aumentar a sincronização celular e, consequentemente, a maturação entre elas. Para isso, foram iniciados testes preliminares para entender qual estratégia garante uma distribuição uniforme dos MXenes ao longo das fibras.

Palavras-chave: Anisotropia, Cardiomiócito, Miocárdio, *Melt electrowriting*, *Scaffolds*

CONTENTS

LIST OF FIGURES

LIST OF TABLES

GLOSSARY

Cellular patch PCL structure printed by MEW embedded in a gel mixture containing GelMA, LAP, and cells in suspension.

ACRONYMS

2D	Two-dimensional
3D	Three-dimensional
ATP	Adenosine Triphosphate
cFBs	Cardiac fibroblasts
CMs	Cardiomyocytes
CNTs	Carbon nanotubes
CPR	Cardiopulmonary resuscitation
CTS	Critical translation speed
CVDs	Cardiovascular diseases
DAPI	4',6-diamidino-2-phenylindole
DMSO	Dimethyl sulfoxide
DNA	Deoxyribonucleic acid
ECM	Extracellular matrix
ECs	Endothelial cells
EDS	Energy dispersive spectroscopy
GelMA	Gelatin Methacryloyl
GNPs	Gold nanoparticles
HA	Heart attack

HCl	Hydrochloric acid
HMSCs	Human mesenchymal stem cells
IHD	Ischemic heart disease
LAP	Lithium Phenyl-2,4,6-trimethylbenzoylphosphinate
MEW	Melt electrowriting
MI	Myocardial infarction
NaOH	Sodium hydroxide
NPs	Nanoparticles
PBS	Phosphate-Buffered Saline
PCL	Polycaprolactone
PFA	Paraformaldehyde
qPCR	Quantitative polymerase chain reaction
RNA	Ribonucleic acid
ROS	Reactive oxygen species
RT	Room temperature
Ru	Tris (2,2' - bipyridine) dichlororuthenium (II) hexahydrate
SEM	Scanning electron microscopy
SPS	Sodium persulfate
UV	Ultraviolet
WHO	World Health Organization

SYMBOLS

P	Air pressure
F	Applied force
ΔL	Displacement
z	Distance from the nozzle to the collector
Ɛel	Elastic limit strain
υ	Elastic strain energy
L0	Initial displacement
θ	Internal angles
ℓ	Side length
Ɛ	Strain
σ	Stress
Et	Tangent modulus
V	Voltage
σγ	Yield point

1. INTRODUCTION

The rise in average life expectancy, coupled to increasingly sedentary lifestyles, announces a potential increase in cardiovascular diseases (CVDs), which are currently the main cause of mortality worldwide [1].

According to the World Health Organization (WHO), even with public health warnings regarding sedentary lifestyles, tobacco consumption and unhealthy diets, cardiovascular diseases still represent an urgent global health problem (Figure 1.), causing approximately 18 million deaths per year [2]. In Portugal, ischemic heart disease (IHD) is the first cause of death, in turn in the Netherlands it is the second, followed by Alzheimer's disease, which corresponds, in both countries, to a large percentage of mortality [3] .

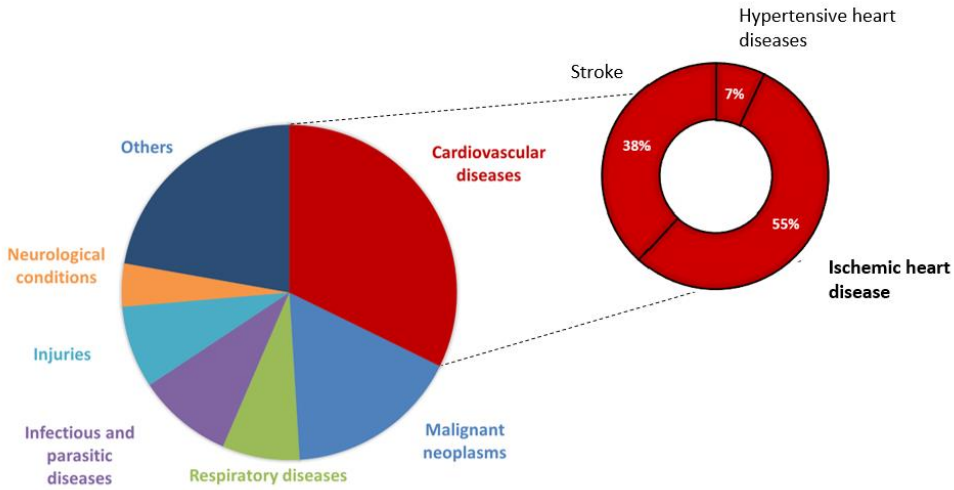

Figure 1 Top 7 Causes of Death Globally in 2019. *Estimate of the main causes of death in 2019 according to the World Health Organization, regardless of age and sex. The graph on the left represents the seven main causes of death at the global level (with emphasis on cardiovascular diseases) and on the right, highlighting the three main cardiovascular diseases, where 55 % are IHD* [3].

IHD is characterized by suppression of blood flow to the cardiac tissue by narrowing or blocking the coronary arteries, which can result in myocardial infarction (MI), commonly called heart attack (HA) [2]. The lack of oxygenation of the myocardial tissue, results in the cellular death of tissue, causing scar tissue, which associated with the weak regenerative capacity of the cardiac tissue can cause the loss of the organ's native functions [4,5].

The heart is one of the most extraordinary organs in our system, besides being the first to be developed during the development of the embryo [6] it is a tissue that is cyclically under mechanical-electrical stress; it contracts ≈ 100.000 times a day [7], propelling oxygen and nutrient-rich blood to remote organs while returning oxygen-poor blood and waste.

Either in a healthy heart and following cardiac injury, mechanical forces and electrical stimuli are essential for cardiac functioning [8], a clear example of the importance of these factors is the performance of cardiopulmonary resuscitation (CPR). During CPR, the force that is applied not only allows blood to circulate through the system, but also stimulates the heart cells. Similarly, the use of defibrillators, which apply a controlled electrical current, helps restore normal heart rhythm [9].

Understanding the organization of the structure responsible for the contractile movement of cardiac tissue, the myocardium, is essential to understand the sequelae of a MI and to develop new approaches for the regeneration of cardiac function through matrices manufactured *in vitro*. The myocardium is a highly organized tissue composed of cardiac muscle cells (CMs), non-contractile cells, and an extracellular matrix (ECM) aligned in specific directions characterized by anisotropic behavior. The effective function of this tissue depends on a coordinated contraction of the CMs and an efficient transmission of electrical signals, both of which are directly related to the aligned structure of the tissue.

Owing to the high socioeconomic burden of keeping patients stable after a MI due to its chronic consequences [10], understanding pathophysiology and treating it is a major priority for cardiovascular research. Currently, the most promising treatment that patients undergo is heart transplantation, which requires surgical intervention, depends on the availability of organs and is still at risk of failure due to an immunological rejection [11]. Despite advances in pharmacological diagnosis and therapy, there is no effective treatment for the regeneration of necrotic tissue function and structure [12].

Therefore, academic work and technological advances, in Tissue and Biomedical Engineering, have been investigating other treatment strategies for this condition. This thesis specifically focuses on the mechanobiological structure of the cardiac muscle, aimed to develop a structure with mechanical parameters similar to native tissue, through an innovative additive deposition technique – Melt electrowriting (MEW) - which will function as a cellular support. To obtain a tissue with well differentiated cells capable of adapting to the heart microenvironment without risking any type of rejection; in this project the mechanical support was tested in different geometries to evaluate its effects on cell organization, alignment, and proliferation.

2. STATE OF THE ART

2.1 Heart Physiology

The heart, the main organ of the cardiovascular system, is composed of contractile muscle tissue responsible for pumping blood along two circulatory systems, the systemic and the pulmonary, which are totally independent because of the four chambers separated by valves that guarantee a unidirectional blood flow allowing the distribution of nutrients and oxygen to the cells, as well as the removal of their metabolic remains [13].

The human heart is located in the thoracic cavity between the second and fifth intercostal spaces in a zone called the mediastinum (Figure 2.A), protected by the pericardial sac/pericardium that separates it from the other structures that are inside the thorax [7].

The pericardium, in addition to surrounding the heart muscle, also allows the protection of the main blood vessels closest to the heart; this is composed of two layers, an outer one, dense and rough fibrous layer of connective tissue that protects the heart and maintains its position in the thorax, and an inner layer that subdivides into the parietal pericardium, joined to the outer layer and the epicardium [7].

In vertebrate living beings, such as Humans, the walls of the heart (Figure 2.B) are defined in three main layers responsible for different functions crucial to the proper functioning of this organ: the endocardium, myocardium and epicardium [14].

The endocardium, the innermost layer, is characterized by a monolayer of endothelial cells that lines not only the walls of the chambers but also the heart valves, allowing direct contact with the blood flow [14], the epicardium is the outermost layer and is made up of mesothelial cells [15], while the myocardium is the intermediate layer composed mainly of contractile muscle cells - CMs.

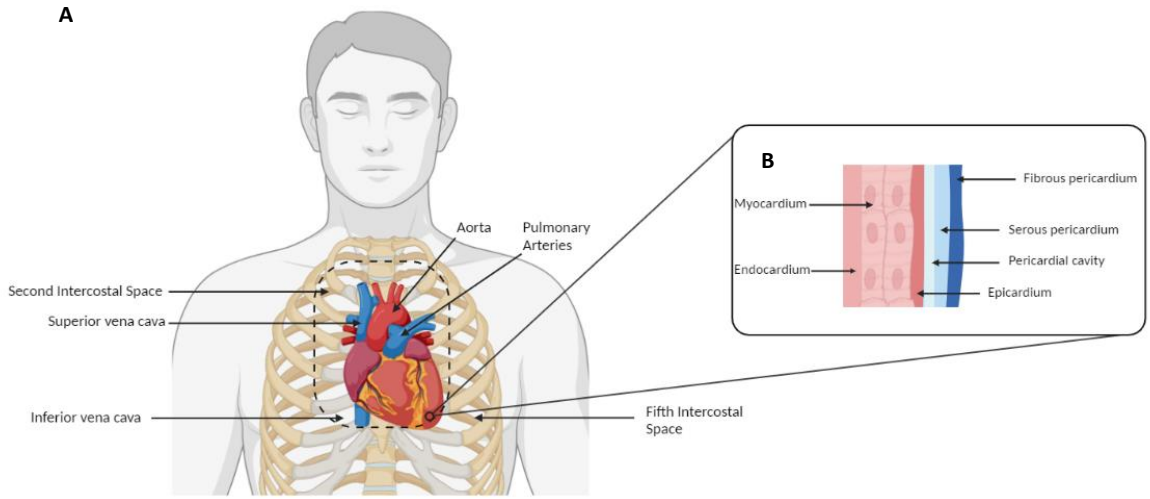

Figure 2 Heart Anatomy. *Representation of the anatomical of the thorax as well as the different tissues that make up the wall of the heart muscle. The figure (A) represents the heart that is located in the mediastinum (dashed line) between the second and fifth intercostal space. The main blood vessels of the organ are also represented: the vena cava (superior and inferior), the aorta artery, and the pulmonary arteries. In (B), the different layers of the cardiac wall are distinguished; from left to right, in shades of pink, is the endocardium, followed by a representation of the myocardium with mono and binucleated CMs and the epicardium; in shades of blue is represented the pericardial cavity, the serous and the pericardium fibrous. Figure created in Biorender and adapted from* [7].

2.2 Myocardium

The myocardium, the middle layer of the heart, is the thickest layer and plays a crucial role in heart contraction [14]. It is made up of several cells and fibers that work together to ensure the efficient functioning of the heart [16].

The main function of this tissue is the contraction of the heart wall [14], which is essential for effective blood flow throughout the body. It is therefore the thickest layer of the heart, with approximately 1.5 cm thickness [17] in its thickest part (located in the left ventricle) since this is responsible for pumping oxygenated blood throughout the body, requiring a significant contractile force [7].

The myocardium consists of layers of CMs that are aligned, in an anisotropic geometry [7], in relation to the ECM, which provides them with essential structural and mechanical support for the contraction of the heart muscle [15].

In addition to CMs, the myocardium contains several non-muscle cells, including endothelial cells, fibroblasts, pericytes, and immune cells (T cells, B cells, and macrophages). These cells perform supportive and regulatory functions within the heart tissue [16].

2.3 Cardiomyocytes

The CMs are the fundamental unit of the myocardium, responsible for generating the force necessary for the contraction of the heart muscle, without any external stimulus [16,17].

Similar to skeletal muscle cells, adjacent cardiac muscle cells are connected by gap junctions, called intercalated discs, electrically interconnecting them, allowing for synchronized muscle contraction and relaxation [18]. Gap junctions allow the CMs to connect, creating long muscle fibers that work as a single mechanical and electrochemical syncytium; this allows the cells to function cohesively and coordinately, involuntarily allowing blood to pump through the circulatory system [19].

Cardiac muscle (Figure 3.A) cells are characterized by the presence of myofibrils inside, which are long filaments, composed of sarcomeres, arranged in series. Sarcomeres (Figure 3.B) are the unit responsible for the process of contracting CMs, composed of two main proteins: Myosin and Actin [20,21].

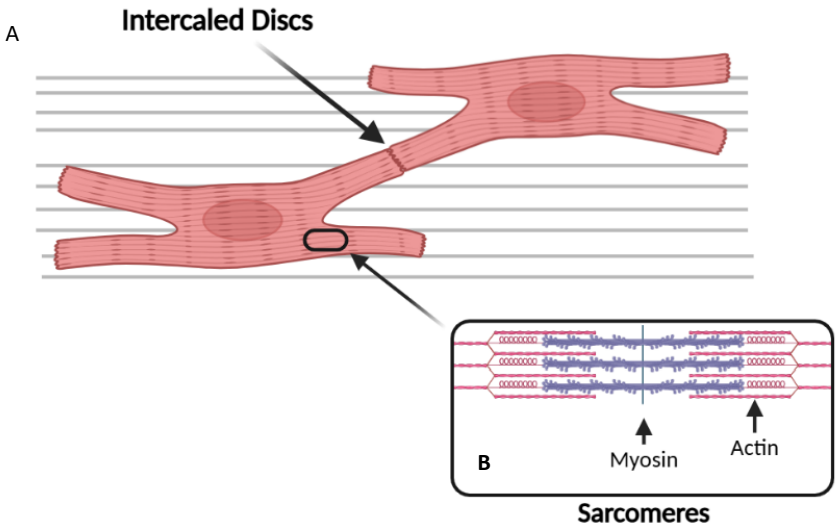

Figure 3 Cardiomyocytes. *Representation (A) of individuals cardiomyocytes interacting with themselves through the intercalated discs and interacting with the ECM. In (B) the sarcomeres are represented, which consist of actomyosin structures (cross-bridges) responsible for the process of contraction of the CMs. Figure created in Biorender and adapted from [20,21].*

Actin filaments, also called thin filaments, are composed of actin, the main protein, tropomyosin and troponin, whose activity regulates the interaction of actin with myosin. In turn, myosin, or thick filaments, have a mobile zone that interacts with actin during cell contractions to form cross-bridges [20].

The synchronized process of cell contraction occurs when an electrical signal generated in the sinoatrial node propagates in the form of an action potential through gap junctions, this potential causes the depolarization of the membrane, opening the calcium channels and allowing the binding of these ions to troponin. The binding of Ca2+, from the sarcoplasmic reticulum to this fine filament regulatory protein, displaces tropomyosin, creating the possibility of binding between actin and the mobile zone

of myosin, forming cross-bridges; cardiac muscle contraction occurs when myosin shifts actin toward the center of the sarcomeres through a process of Adenosine Triphosphate (ATP) hydrolysis [20].

In addition to this major process, the inner layer of the cardiac wall, the endocardium that connects to the myocardium through connective tissue, is also shown to play a role in the contractile activity of the cardiac muscle by secreting vasoconstrictors, the endothelin, which regulate ionic concentrations in the surrounding fluid [7].

Despite the high physiological regulation associated with CMs, the contractile function of the cardiac muscle is highly dependent on the ECM that mechanically supports this tissue and the anisotropic behavior that is inherent to it [22].

2.4 Anisotropic Structure

2.4.1 Cardiac Motion

The movement of the heart muscle is naturally continuous, coordinated, and cyclical, where the organ is contracted and deformed, in a synchronized way, to create a torsional movement, that is, a rotation around the longitudinal axis, optimizing the pumping of blood in the blood system. This coordinated cycle depends essentially on two main reasons, the cellular and mechanical environment in the myocardial tissue and the anisotropic behavior that this tissue exhibits [22,23].

2.4.2 Extracellular Matrix Properties

Endothelial cells (ECs) and cardiac fibroblasts (cFBs) are the most numerous non-myocyte cell types in cardiac muscle; ECs are responsible for tissue nutrition through the capillary network that characterizes them and cFBs are the fundamental unit of the cardiac extracellular matrix [16].

The cardiac ECM is a complex and dynamic structure that confers fundamental mechanical properties to cardiovascular tissues, in response to different stimuli being one of the components responsible for myocardial contraction and electrical conductivity [24].

ECM is composed of a mixture of fibrillar proteins (collagen) and non-fibrillar components (sheet-forming protein polymers) [24] such as glycoproteins and proteoglycans, which provide structural support to myocardial cells and maintain a favorable cellular environment for the transmission of electrical signals and coordination of CMs contraction, [16,25] further facilitated by the presence of blood capillaries and nerve fibers connected to the matrix.

The complex glycoprotein network is then converted into myocardium-specific mechanical properties, essential to the cardiac cycle, resulting in a Young's modulus of the myocardium of approximately 200−500 kPa at end-diastole with a strain between 15-22 %, about 10−20 kPa at end-systole with a

strain inferior a 10 %, and about 3−15 kPa at tensile strength, which corresponds to the stress limit that the tissue withstands before deforming [16,22].

Although the ECM plays a crucial role in the contraction of the heart muscle, the cardiac cycle is also dependent on its anisotropic behavior, derived from its alignment and the orientation of the cells [16].

2.4.3 Anisotropic Behavior

Anisotropic behavior is defined by the variation of properties according to the established direction, promoting different mechanical qualities [26]. The myocardium, at the macroscopic level (Figure 4.A) has layers oriented at specific angles, organized anisotropically, which allow different parts of the myocardium to contract in a coordinated way, generating efficient forces for its contraction [27]. At the cellular level (Figure 4.B), the way in which CMs are connected and form muscle fibers through intercalated discs also has an anisotropic orientation, in relation to ECs and cFBs [27,28].

Heart cells are dispersed swirl and spiral around the chambers of the heart, in a helical pattern [7], mainly due to the alignment of the ECM, which builds different orientations in the layers of the heart wall, this factor is responsible for the torsional movement that occurs during the heartbeat. Bray et al, show that cardiomyocytes are highly influenced by the external environment in which they are found, especially by ECM. Through the culture of neonatal CMs with different fibronectin concentrations; sarcomeres and myofibrils exhibited a greater degree of alignment in cultures with higher concentrations. Fibronectin, as one of the glycoproteins most present in the ECM and responsible for cell adhesion, thus reveals that the CMs are aligned by geometric stimuli [22,23].

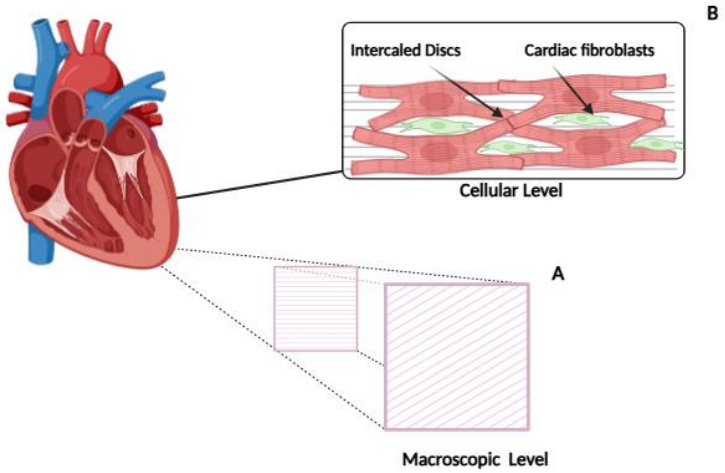

Figure 4 Anisotropic Structure of the Heart. *Representation of the anisotropic structure of the heart. (A) represents the different orientations of the myocardial fibers along the cardiac wall and (B) represents the cell alignment along the ECM. Figure created in Biorender and adapted from [21,22].*

The anisotropy present in cardiomyocytes directly affects their functions; by changing the size and shape of the intracellular cytoplasm, which ends up directly influencing the alignment of the sarcomeres along a unidirectional axis [22].

In addition, this anisotropic organization significantly influences the transmission of electrical signals by the cells, the gap junctions are thus polarized to the ends of the cells, thus increasing the connection between them, which in turn is essential for the coordinated contraction of the muscle [22,27].

The impact of cardiac anisotropy function on contracting and pumping blood efficiently is therefore connected to vast factors from the internal structure of cells and their adherence to the ECM, to the macroscopic geometric characteristics of the entire cardiac muscle [21,22,27].

The detailed knowledge of this structure and consequently its effect on the functions of cardiac biomechanics, can be very useful for the design of functional biomaterials capable of mechanically replacing the necessary support for cardiac tissue in case of loss of function due to MI.

2.5 Pathophysiology Myocardial Infarction

The clinical diagnosis of a MI is complex because it requires several tests, such as electrocardiograms, visualization of tissue images and the detection of specific biomarkers for proteins related to the death of cardiomyocytes [10].

At pathological level, this condition is defined by the death of CMs resulting from a lack of oxygenation and nutrient supply due to an ischemic insult (Figure 5.) [4,5].

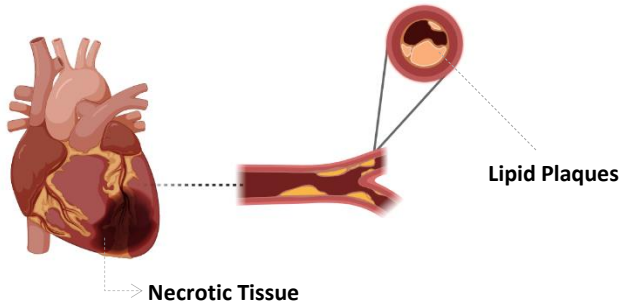

Figure 5 Myocardial infarction. *Representation of a heart with necrotic tissue after an MI due to a blockage of blood flow as a consequence of the accumulation of lipid plaques derived from atherosclerosis. Figure created in Biorender.*

IHD is a condition characterized by reduced and/or interrupted blood flow to the heart muscle, due to blockage of the coronary arteries, that supply oxygen and nutrients to the cardiac tissue. Stopping this flow can result in chest pain (angina), heart attacks, such as myocardial infarction, and other long-term heart problems, such as heart failure. The blockage of the arteries, in most cases, is a consequence of atherosclerosis; this is a chronic and progressive condition that involves the accumulation of lipid

plaques, inflammatory and smooth muscle cells, as well as necrotic cell debris, in the inner endothelial layers of the arteries [29].

The CMs, from mammalian animals, when suffering from ischemic disease, are able to maintain their contractile capacity thanks to the phosphate reserves they have stored. However, the generation of inorganic phosphate and intracellular acidosis decrease the binding of calcium to contractile proteins, thereby activating functional depression mechanisms, which can lead to impaired contractility and long-term weakening of myocardial cells. If blood flow is restored within the first 5 minutes, the possibility of recovery from the full damage is highly likely; however, tissue damage after an average of 20 minutes may be permanent [10].

Some consequences of the delay in restoring blood flow may be reversible, such as the oxidation of contractile proteins through reactive oxygen species (ROS) and the functioning of these proteins by the dysregulation of calcium channels; however, prolonged oxygen deprivation on CMs can also lead to cell death, damaging myocardial tissue in proportion to the number of dead cells [10].

The death of CMs after infarction occurs mainly in the first 24 hours due to necrosis, an unscheduled cell death characterized by breaking the integrity of cell membranes and triggering pro-inflammatory processes in the surrounding area, also cellular hypoxia and cellular-biomechanical tension activates intrinsic and extrinsic apoptotic pathways [10].

In addition, the ECM, which plays a key role in supporting CMs, is also affected as a response to a myocardial infarction. In response to inflammatory stimuli, metalloproteins are released, which are responsible for degrading the proteins that make up the ECM. However, this structure is not only essential for cellular support, but also for the regulation and stimulation of a desirable functioning of CMs. At the same time, to compensate for the damaged ECM, a provisional matrix is formed, primarily composed of fibrin and fibronectin, which are essential for providing structural support, promoting cell adhesion, and facilitating tissue regeneration [10].

Unlike smooth and skeletal muscle tissues, the regeneration of cardiac muscle tissue, a process aimed at replacing the damaged myocardium with viable functional tissue, is very slow and limited, with a regeneration rate of only 1 % per year, which makes its self-regeneration impossible, contributing to the progressive degeneration of dead tissue [4,5,20,30].

The cellular regeneration of CMs is essential for the functioning of the heart muscle, which in turn is responsible for pumping blood throughout the body; this slow self-process of regeneration severely affects the health of any individual. In this sense, the formation of structures that simulate the native environment of the heart, promoting and reinforcing the automatic regenerative process of the myocardium, is essential for the development of treatment for patients suffering from this type of medical condition.

2.6 Tissue Engineering

During a MI, thousands of viable CMs lose their functionality and consequently the myocardium also loses its native structure.

Due to the lack of cell division capacity of the CMs and even though there are some stem cells in the heart muscle, the regeneration process is not effective, therefore, the healing process kicks in, where the native tissue has been affected [10,31]. This process, although essential to maintain the integrity of the tissue, does not acquire its contractile and conductive properties, not allowing the contractile functioning inherent to the organ [31].

In therapeutic terms, the main objective will be to prevent the formation of scar tissue in the damaged area or replace this tissue with new functional tissue. In this sense, several techniques and devices have been developed, focusing on mimicking the cellular environment of the heart muscle, in the areas of cell therapy and cardiac patches [10].

2.6.1 Prior Treatments

The approach of cell therapy and tissue engineering, although overlapping, are different concepts. Cell therapy consists of administering a suspension of cells with the aim of regenerating, or rather improve, an existing tissue [32]. In turn, tissue engineering is a concept where are formed new functional tissues, which are produced extra-organism; these fabrics are constructed with specific sizes, geometries and functions [31,32].

Cell therapy, typically given by intravenous injection, aims to repair the cardiac functions of damaged CMs with the use of various types of cells [31]. Initially, non-cardiac cells were used, such as Skeletal Myoblasts and Bone Marrow-Derived Cells, which, despite being effectively applicable and stable, did not create an adequate electrical-mechanical connection and presented some instability, respectively [33,34].

Later, cells that derived from heart tissue were used. Both, cardiac stem cells, capable of expanding and self-regenerating, as well as induced pluripotent cells capable of differentiating into any cell type and expanding *in vitro*, were not mature enough to fulfill the functions required by native tissue [35].

Each cellular microenvironment has its own needs, both in terms of oxygenation and nutrition, and in maintaining a stable waste stream; cell studies, although promising, showed poor adaptation of cells to the native tissue and their environment, failing to recover the myocardium [31]. Thus, therapy by stimulation of paracrine factors arises.

Paracrine factors are factors secreted by the cell, which act on neighboring receptors of nearby cells. These molecules promote intercellular communication, which in turn promotes the regulation and regeneration of the cells themselves within their microenvironment. In order to obtain these

regenerative effects, the administration of growth factors, non-coding ribonucleic acids (RNAs) and extracellular vesicles, such as those containing paracrine factors, was tested [36].

The results, although once again positive, are still not enough to move forward with a clinical treatment, since it has a limited duration and distribution. This is where tissue engineering comes in, an approach not only focused on understanding cellular responses to drugs, but also on recreating as closely as possible the cellular environment in which they develop. In this sense, research is developed by the manufacture of cardiac patches, which may or may not contain cells and/or active factors. In general, these devices have the main function of providing structural support to cells, enhancing their development [37]. However, to restore the integrity and function of the myocardium, it is necessary to understand how the intracellular interaction occurs, and between the cells and the ECM itself, in order to produce patches as similar to as possible.

Due to the anisotropic characteristics of cardiac muscle tissue and the peculiar electrical transmission between cardiomyocytes, one of the main objectives in tissue engineering will be to build a mechanical and electrical system with the characteristics of native tissue, promoting cell maturation, ensuring that the cells produced *in vitro* will adhere positively to the organ.

2.7 Scaffold Production: Design and Fabrication

A scaffold-based tissue engineering strategy consists of a programmed structure where viable cells and factors that promote self-repair or regeneration of damaged tissue are combined. This structure has as its main functions the organization and support of cells, their growth and also their maturation and differentiation into cells corresponding to the native tissue [38].

In this sense, scaffolds have to meet some requirements to be able to be tested. Its stiffness and mechanical strength must be able to replace the mechanical function of the damage tissue, which does not imply that it is necessarily the same as the original tissue. In addition, its design must be beneficial to cell adhesion, allowing cells to migrate, grow and develop in natural metabolic processes. Also, the size of the structure itself must be appropriate, so as not to harm the healthy tissue around the damaged area and so that it can be adapted to each patient in case of need [39].

In clinical terms, these structures have to meet sustainable requirements in terms of costs and reproducibility capacity, as well as undergo a thorough quality control [40].

2.7.1 Design

The design of each scaffold is adapted to the type of fabric and its function, but some basic criteria have to be met, such as a suitable form, a temporary support, having the ability to promote the formation of the new fabric and being able to adhere to the native fabric. Although it is difficult to evaluate all these criteria directly, it is possible to control some parameters that allow the structure to have

the desirable standards, such as material composition, porosity, structural mechanics, surface properties and degradation properties [40].

Pore size and porosity are concepts that are related to and directly linked to the mechanical properties of scaffolds. Although they are different concepts, both are very important in the production of structures; a pore can be defined as a void space within a scaffold, whereas porosity can be considered as a collection of that pores. They are defined as macro pores when they have a diameter between 50 µm and 200 µm and a porosity of more than 70 %, while a micro pore only has dimensions between 1 and 1000 nm in diameter [41].

Structures with porosity can also be classified according to the connection of their fibers, into two groups: the interconnecting (open pores) and the non-connecting (closed pores) [38]. This is a critical factor in the production of scaffolds; if a structure is porous but does not present a high interconnectivity (100 % interconnecting per volume is desirable), the scaffold will not be functionally relevant, not presenting an effective ability to support the cells and allow their migration and, consequently, their expected organization [41].

In cardiac tissue, the scaffolds that are produced must have a highly porous matrix (above 90 %), with pore sizes greater than 50 µm and with a high interconnectivity assured, which will provide good cellular support and facilitate the process of vascularization, which means, the penetration of blood vessels, into the recipient tissue [42].

2.7.1.1 Morphology Analysis

The need to produce these highly porous structures for the regeneration of cardiovascular tissue presents challenges from a biomechanical point of view during the manufacture of scaffolds [39]. In this sense, the characterization of the structures is essential to assess their porous quality and, thus, approve their use in the cardiac context. Microscopic visualization plays a crucial role in characterizing these structures, allowing for detailed morphological analysis.

Scanning electron microscopy (SEM) stands out as it allows for nanometric and three-dimensional visualization of samples [43]. This technique is characterized by the emission of an electron beam to the surface of the sample, where the resolution of the image is dependent on the applied voltage. The interaction between the beam and the sample is detected, providing detailed images of the sample's shape, roughness, and composition [44].

Thus, SEM allows for the acquisition of high-resolution images that are essential for analyzing the distribution and interconnectivity of pores, ensuring that the design and structure produced meet the requirements for application in cardiac tissue engineering.

2.7.2 Manufacturing

Printing technology is an area whose development has escalated in recent decades, advancing from traditional two-dimensional (2D) printing to additive printing, in which a three-dimensional (3D) object is built by adding multiple layers [45,46]. The fabrication of 3D structures has been used for applications ranging from everyday life to education and science, with a main focus on its use in medical applications with the production of scaffolds for tissue transplantation [45,46].

As relevant as the selected biomaterial itself is the way it is printed; there are many choices of manufacturing methodology, but many are irrelevant to the goal of building a 3D structure with a specific material and architecture for the application of cells [47]. Although many techniques such as solvent casting, freeze-drying, gas foaming, and electrospinning are considered classical methods with limited relevance to tissue engineering, they serve as the foundation for newer techniques that aim to replicate the cellular microenvironments of tissues (Tabel 1). One such technique is MEW, an additive manufacturing process designed to meet the specific demands of tissue engineering [45,46,47].

Table 1| *Overview of classical methods of fabrication and of MEW providing a comparison of their operation modes, as well as the advantages and disadvantages of each technique.*

Printing Technique	Operation Mode	Advantages	Disadvantages	References
Solvent Casting	Solvent is evaporated and creates a porous matrix.	Some control of pore size. Porosity can reach 90%.	Use of highly cytotoxic organic solvents.	47
Freeze Drying	Polymer solution is frozen and the solvent is sublimated.	It produces very connected and porous structures.	Pore size is not controlled, involves the use of toxic solvents and spend a lot of energy.	45,46
Gas Foaming	Polymer is saturated with CO2 at high pressure.	Does not require the use of toxic solvents.	Pores do not have a high interconnectivity.	45,46
Electrospinning	Polymer solution is subjected to an electric field that creates a jet where the solvent is evaporated and forms a random mesh.	Fibers produced are extremely thin which allows for a high surface-to-volume ratio.	Toxic solvents may be used and do not allow the manufacture of precise architectures.	45,4647
Melt Electrowriting	Polymer is melted and ejected under pressure and an electric field, where the fibers are deposited in a controlled manner.	High deposition accuracy, allows controlled stacking of the fibers and creation of complex 3D structures without the use of solvents.	The formation of porous structures with reduced diameters is dependent on a great optimization of the printing parameters.	47

2.7.2.1 Melt Electrowriting

MEW is a nozzle-based additive manufacturing method with micro and nanoscale production capacity. The goal of additive manufacturing in biomedical engineering is the production of scaffolds with precise morphologies, using specific materials, to fabricate anatomically shaped implants [48].

The great advantage of this printing technique is the direct use of molten polymers without the need to use solvents; that way, the accumulation of liquids is prevented, and the use of toxic solvents is avoided. In addition to scaffolds being complex to design, they can also be produced without the use of ventilation systems and their use can be immediate [49].

A MEW machine (Figure 6.) contains of a printing head equipped with a heating system attached to a syringe moving in the x and y directions plane, when a layer is built the platform moves one step in the z direction to create the next layer [50]. The printing process consists of the deposition of fibers sequentially and stacked in a collector through the use of electric fields, variation of pressure and voltage used [51,52].

More specifically, first, the molten material is extruded through a nozzle using air pressure and then a drop forms at the tip of the needle; the high voltage applied creates an electrostatic attraction in the droplet, where a cone is formed, called the Taylor cone.

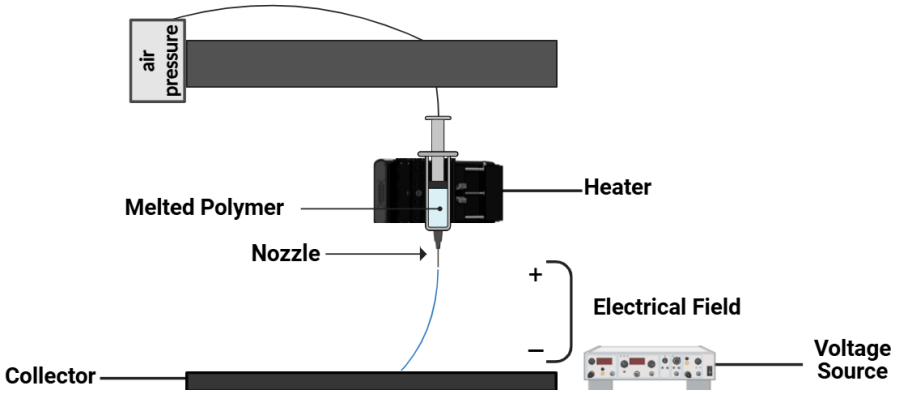

Figure 6 MEW Printer. *Representative figure of melt electrowriting process, where the deposition of a molten polymer through a nozzle is observed under the effect of an electric field and an applied pressure, allowing the controlled formation of fibers on the surface of the collector. Figure created in Biorender and adapted from [51].*

The taylor cone is considered a signature of manufacturing quality in MEW. It is formed by the interaction of the molten fiber with the electric field, and it is strongly dependent on the pressure and distance from the nozzle to the collector, after stabilizing its shape, the molten material jet allows the fabrication of structures with high precision. For the stabilization of the taylor cone (Figure 6.), it is necessary to lower the applied pressure and/or increase the electric field, depending on the viscoelastic properties of the material used. Maintaining these conditions over time is essential and at the same time the challenge is avoid fluctuations in the stability of the jet [53,54].

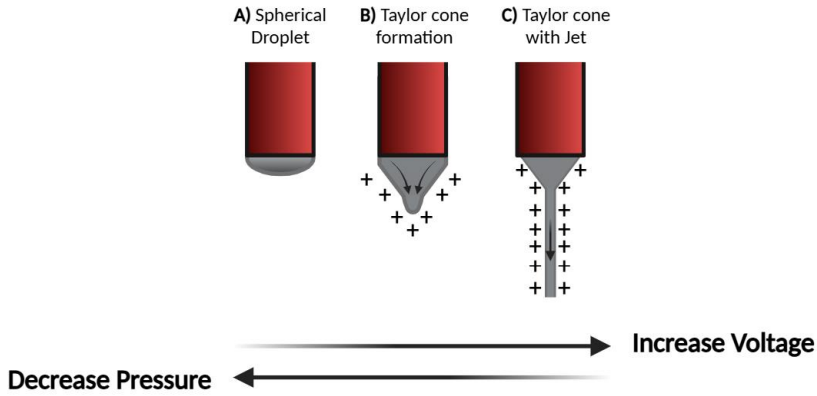

Figure 7 Taylor Cone Formation. *Representative figure of the taylor cone formation with the increase of the applied voltage and/or with the decrease of the pressure. In (A) the beginning of the extrusion process is represented, when the polymer is only under the effect of the applied pressure, in (B) the polymer begins to be under the effect of the electric field and the Taylor cone begins to form, finally in (C) the polymer is already being extracted totally under the effect of the applied voltage where a jet is formed to the collector. Figure created in Biorender and adapted from [54].*

After the jet stabilizes, the developed fiber is deposited in the collector, following a programmed path which is based on software model. This manufacturing technique depends on several parameters, such as the temperature of the polymer, the pressure (P) used, the speed (S) used, the distance to the collector (z) and the applied voltage (V), responsible for stabilizing the jet, avoiding Plateau-Rayleigh dispersion, which causes a movement colloidal fiber [52].

The colloidal movement of the fiber happens in all polymer flows from the nozzle to the collector, but for each flow, there is a critical translation speed (CTS), where the fiber deposition changed from coiled to linear and the jet becomes straight lines [50]. CTS occurs at the time when the nozzle movement speed is greater than the contact speed between the fiber and the collector [55] and it may be essential to use it to produce certain types of designs.

The use of high temperatures for this printing structures is only possible by the use of thermoplastics, due to their thermal reversibility capacity, which allows them to be heated and cooled multiple times; they also have mechanical properties such as their elasticity, flexibility and high strength [56].

One of the most widely used thermoplastics in MEW is polycaprolactone (PCL) [57], which is capable of being manufactured in a reproducible way, bring multiple advantages to tissue engineering [57, 58]. PCL is a biocompatible and synthetic polymer [57] with a semi-crystalline structure that allows it, up to its voltage limit, to be flexible and rigid at the same time [57,59].

PCL has several mechanical properties that allow it to be one of the most used biopolymers in this type of additive manufacturing, of which its relatively low melting temperature, between 58 °C and 65 °C, that allows it to be easily printed and to have a fast cooling and solidification process of the scaffolds [59].

An essential requirement for the development and maturation of cardiomyocytes is a physical support such as ECM in its native state [31]; through this bottom-up technique it is possible to fabricate a precisely design and organized 3D scaffold capable of mimicking the architecture of the myocardial ECM and its mechanical properties [60].

Previous geometry studies reveal that meshes with a rectangular pattern have mechanical properties similar to native tissue, and promote cellular alignment along the contour, however, the deformability limitation was not compatible with the anisotropic cycle of the heart [4]. Recently, scaffolds formed with an organized hexagonal geometry exhibit a biaxial structure, which results in an effective anisotropic structure for the proliferation and maturation of hiPSC-CMs [52].

2.7.2.2 Mechanical Characterization

Thermoplastic polymers, which can be extrusion molded when melted, can be amorphous or semi-crystalline; amorphous polymers exhibiting minimal elasticity below their glass transition point, while semi-crystalline materials exhibit some degree of elasticity [56,61].

The duality of the composition, between hard and soft segments, of semi-crystalline materials allows them to deform under stress and return to their original structure when the stress is removed. Its flexibility and resistance make this type of material widely used in biomedical applications, in particular, in cardiac tissue, the mechanical resistance of the manufactured structures is essential so that there is no risk of degradation during the cyclic movement of the myocardium [25,61]. The mechanical properties of semicrystalline thermoplastic polymers are characterized by a stress-strain curve (Figure 8.), which is characterized by two main zones, the elastic and the plastic [61].

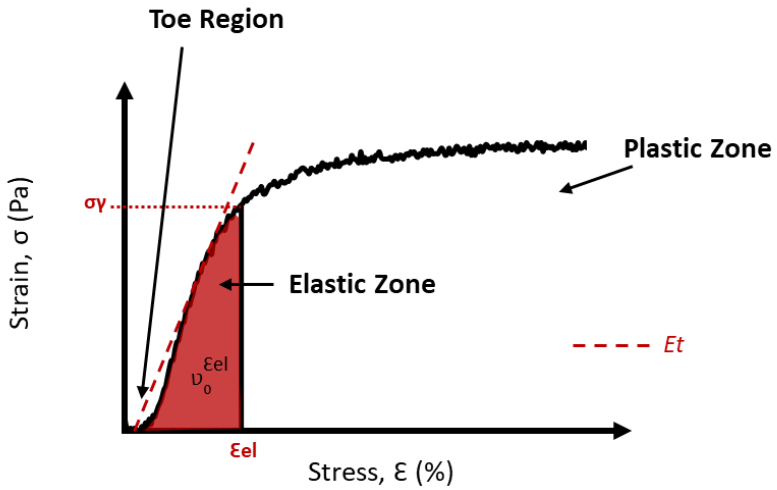

Figure 8 Stress-Strain Curve of Semi-Crystalline Materials. *Representation of a stress-strain curve characteristic of semi-crystalline materials. The curve is divided into two zones, elastic zone and plastic zone. In red is represented the mechanical parameters, namely yield point* (σγ)*, tangent modulus (Et), elastic limit strain* (*Ɛel) and elastic strain energy density* (*υ). Figure created in Biorender and Canva and adapted from* [4,61].

At the beginning of the curve there is a characteristic zone, usually of soft tissues, but also of structures manufactured with hexagonal geometries, the toe region, which is defined by a deformation practically without the application of stress, which corresponds to the phase where the material realigns before entering in its elastic phase. The elastic phase, the second in the deformation of a semicrystalline material, is defined by a deformation proportional to the applied stress; during this phase when the stress is taken away the material can return to its original structure [61]. In turn, when the applied tension is high, the material can reach its plastic deformation, which is irreversible even when the structure is no longer under stress. The plastic behavior starts at the Yield Point (σγ), which is the stress point where the deformation of the material can no longer recover its original shape, and ends at the break point, where the definitive rupture of the material occurs [61].

In addition to this, it is possible to extract several essential information for the mechanical characterization of scaffolds, such as: elastic limit strain (Ɛel), tangent modulus (*Et*) and elastic strain energy density (ʊ). The elastic limit strain is the maximum point of elastic strain that a material can reach, while the modulus tangent characterizes the stiffness of a material. In turn, elastic strain energy is the energy that the material is able to store during elastic deformation [61,62].

2.8 MXenes

In the last years, in cardiac tissue engineering, there has been a focus on the production of responsive polymers combined with conductive materials to develop electrically conductive scaffolds [63,64]. Some materials such as gold nanoparticles (GNPs) and carbon nanotubes (CNTs) have been studied in this sense [65].

GNPs, despite having a high biocompatibility, they have difficulty in remaining stable over time without a reducing agent, which leads to their agglomeration and alteration of their properties [66]. On the other hand, despite CNTs significantly increasing electrical conductivity, the difficult biodegradability of these NPs makes their use limited by rich toxicity [67].

In this sense, MXenes emerge as nanoparticles (NPs) with extreme electrical conductivity, significant biocompatibility and the ability to adapt to different materials such as patches and hydrogels [68]. As MXenes are 2D NPs, shaped like sheets, with a high level of conductivity, high surface area, and functionalize surfaces, which makes them a target of interest for several areas such as drug delivery, medical imaging, biosensors and tissue engineering [69].

The general formula of these particles is Mn+1XnTx (n = 1, 2, 3, or 4), where the M stands for an early transition metal, the X can be carbon and/or nitrogen and the T represents the functional group such as: -O, -OH, halogens, or chalcogens [64,69].

The versatility that these 2D particles present on the surface makes it possible to create a favorable environment for cellular interactions [63], which can promote cell proliferation and maturation in a scaffold. In addition, the thickness and flexibility of MXenes allow 2D sheets to wrap around polymers and fibers cohesively [63, 69].

MXenes have also been shown to have a reduced immunogenicity, which reflects a low probability of activating the immune system and creating an adverse reaction of the native organ [69]. PCL is a synthetic and inert polymer, so it can be predicted that the addition of these particles, could be challenge, but would improve the functionalization of scaffolds.

In particular, the regeneration of cardiac tissue requires electrical interaction between cells, in order to ensure normal physiological function, Basara.G et. al. demonstrates that the addition of MXenes to hydrogels improved the synchronized beating of cardiomyocytes derived from human induced pluripotent stem cells [68]. In addition, MXenes integrated into PCL fibers has already proven to be effective in relation to the adhesion and proliferation of human dermal fibroblast cells.

AIM OF THE THESIS

Driven by the goal of regenerating cardiac tissue damaged after a myocardial infarction, we developed cellular structures that mimicked the native cardiac tissue microenvironment.

This project aimed to optimize the process of developing 3D PCL scaffolds with different geometries that varied in pore size and internal angle; to test their mechanical characterization to assess if they resembled the native myocardium, with an emphasis on anisotropic behavior, tensile strength, and elastic capacity. Additionally, another goal was to understand how the different scaffold geometries, functioning as cellular support, shaped cell orientation and alignment. In this regard, an efficient method to encapsulate human mesenchymal stem cells (hMSCs) in Gelatin Methacryloyl (GelMA) was initially optimized, and their viability was assessed. Subsequently, cell proliferation was visually evaluated through nuclear staining, and their alignment was analyzed via F-actin staining using confocal microscopy.

Since the future aim is to translate these structures into clinical applications as a treatment for MI patients, it was conceived as an effort to further improve communication between cardiomyocytes (CMs) by integrating NPs into the hexagonal PCL structures. With this in mind, one of the objectives was to uniformly adhere conductive NPs to the PCL fibers to create a current within the scaffold, enhancing cellular communication and synchronization.

3. MATERIALS AND METHODS

3.1 Materials

PCL sterile granular	PC12 Medical Grade, Batch 7500233492, Corbion, NL
Gelatin methacryloyl	GelMA, G2500-500G, Sigma-Aldrich, USA
Methacryloyl anhydride	L14357.18, Thermo Fisher Scientific, USA
DMEM (1X)	DMEM (1X) + GlutaMAX medium with 4.5 g/L D-Glucose and Pyruvate, 31966-021, Gibco, USA
Ru solution	Tris (2,2' - bipyridine) dichlororuthenium (II) hexahydrate, 50525-27-4, Thermo Fisher Scientific, USA
SPS solution	Sodium persulfate, 7775-27-1, Thermo Fisher Scientific, USA
LAP solution	Lithium Phenyl-2,4,6-trimethylbenzoylphosphinate, 85073-19-4, Merck Life Science, NL
PrestoBlue	PrestoBlue Cell Viability Reagent, A13261, Invitrogen, Thermo Fisher Scientific, USA
PFA	Paraformaldehyde, 50-00-0, Thermo Fisher Scientific, USA
Triton X-100	9036-19-5, Merck Life Science, NL
DAPI	4',6-diamidino-2-phenylindole, 28718-90-3, Merck Life Science, NL
Phalloidin 550	17466-45-4, Merck Life Science, NL

3.2 Scaffolds Manufacturing

In order to produce scaffolds with anisotropic architecture, PCL was melted and printed through an in-house developed MEW printer.

3.2.1 Design

The scaffolds were printed with hexagonal geometries, in order to obtain a cell support structure with anisotropic behavior. For this purpose, a Python script was written (Figure SI.1) that generates the G-code which will be interpreted by MEW printer. The G-codes generated were previously observed in the NCViewer software, before each print.

The hexagonal architectures (Figure 9.) that were tested, were designed with different geometries, in which the side length differs (ℓ) 400 µm and 600 µm, and all of them with internal angles (θ) of 30 °, 45 °, and 60 °.

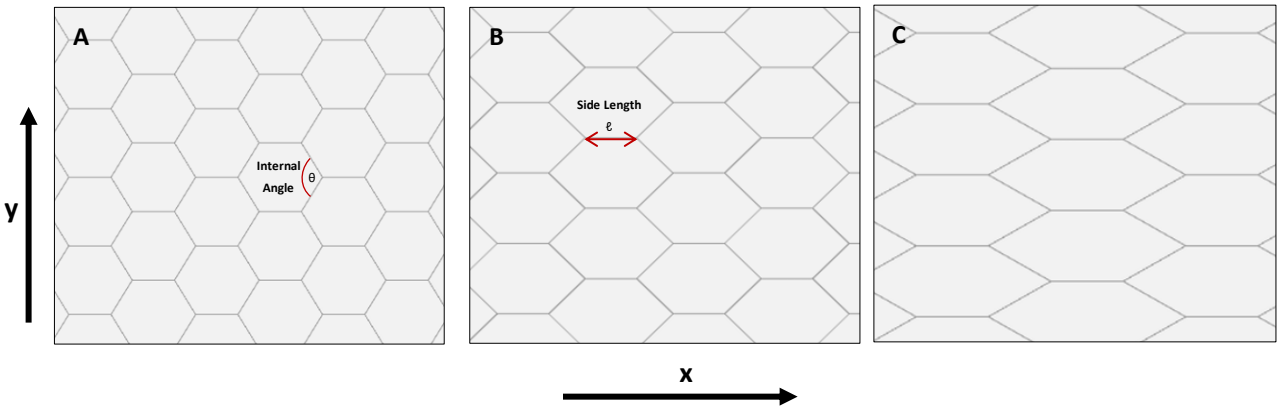

Figure 9 Hexagonal Geometries Patterns. *Representation of the three geometric patterns with hexagonal structures drawn in python script designed for the manufacture of scaffolds. In (A) hexagonal structures with an internal angle of 60 º are illustrated, in (B) a hexagonal architecture with an internal angle of 45 º and image (C) represents a structure with a hexagonal geometry with an internal angle of 30 º. In (A) the internal angle (*θ) is represented *and in (B) the side length (*ℓ). *Figures taken from NCViewer software.*

3.2.2 Optimization of Printing Parameters

The PCL was melted, without the use of solvents, at 110 °C by a power supply heater (TBL 090-124, Traco Power) while inserted in a glass syringe with a 25 g diameter 0.5 mm needle (FISNAR, EUROPE). The syringe is attached to the print head, which in turn is connected to an air pressure system.

This entire system is initially calibrated in the three-dimensional axes x, y and z; on the vertical axis, it is necessary to set the point (X,Y,0) at the point of contact between the nozzle and the collector glass, in order to prevent contact between them.

The PCL, already molten, is pushed through the air pressure, and then subjected to a high-voltage electric field where it is directed to the collector (x-y surface) controlled via an advanced 2-axis stepper motor controller ("head printer").

Printing parameters such as the applied air pressure (P), the voltage (V) to which the polymer is subjected and the distance from the nozzle to the collector (z) were tested multiple times and consecutively to obtain the best possible fiber deposition, depending on the desired design.

After defining these parameters, it is necessary to find the value of CTS [1], in order to be able to control the deposition of the fiber more accurately. For this purpose, profiles speed fibers were printed with the parameters defined constant, where the speed change throughout the printing process according to a Python script (Figure SI.2). The range of values used in the print parameters is shown in the table below (Table 2).

Table 2| *Values of the main parameters optimized in MEW printing that were used for the different pore size.*

Side length (ℓ) µm	Pressure (P) bar	Collector distance (z) mm	Voltage (V) Kv
400	1.00	2.00	4.60 – 4.90
600	1.00	2.00	4.20 – 4.70
1000	1.00	2.50	3.70 – 4.00

3.3 Scaffolds Characterization

Before scaffolds have been used in biological tests, it is necessary to understand whether the optimization of the printing technique reflects the formation of structures with the necessary requirements both at the morphological and mechanical level [42].

3.3.1 Measuring Printing Accuracy

The morphological evaluation (printing accuracy) of the printed scaffolds was done by capturing images through a digital microscope (5000x resolution, VHX-500F, KEYNCE, Japan). The captured images were taken at a 90 ° angle by the equipment itself in order to ensure accurate measurements of the structures.

The images acquired by VHX Software were used to evaluate the quality of the external and internal structure of the printed scaffolds, with a main focus on the pore areas and the internal angles formed. The quantitative analysis of these morphological characteristics was performed using the ImageJ software. The measurement of the pore areas is carried out automatically by making a threshold of the

[1] It is important to note that the printing parameters may change with the room temperature and humidity.

images that are previously altered in brightness, contrast and color; in turn, the internal angles were measured manually through the *angle tool*.

The print quality (Q range) is then evaluated by comparing the measured area (A measured) and the expected area (A expected), by equation 1; where 1 (100 %) is defined as the value that represents a perfect alignment of the scaffolds and 0 as a structure with a random alignment:

$$\mathrm{Qrange} = \frac{\mathrm{Ameasured}}{\mathrm{Aexpected}} \, , 0 \, < \mathrm{Qrange} < \, 1 \qquad 1.$$

3.3.2 SEM Characterization

The microstructures of the scaffolds were analyzed using SEM (200000x resolution, FEI QUANTA 600F). The images acquired were obtained in high vacuum with voltage between 2.00 Kv and 5.00 Kv and a spot of 3.00. To obtain the images, by xT microscope control software, with the best resolution, the alignment of the lenses, the beam shift, the contrast and the luminosity were changed with the increase in magnification.

Through these images it was possible to assess the real size of an isolated fiber and the stacking of the fibers that form the wall of the scaffolds, as well as to confirm the interconnectivity between them.

3.3.3 Uniaxial Tensile Tests

To evaluate the mechanical properties of the scaffolds produced and ensure that they have properties comparable to those of the native tissue, the scaffolds with different designs were subjected to uniaxial tests on a tensile tester (BioTester 5000, Cellscale, Canada) in both x and y directions , at room temperature (RT); these data were collected through the LABJOY software. For this analysis, structures with internal angle of 45 ° were discarded due to similarity with structures with internal angle of 60 °.

The scaffold dimensions should be reported that are previously cut with the use of small blades or with a scalpel, measured and weighed are tested with 2.5 N load cell capacity for a stretch magnitudes of 600 % (which means a 6 x initial displacement *L0*). The stretching process ends at 400 seconds or when the scaffolds have reached the maximum defined displacement: 40000 µm. To monitor the deformation of the structure over time, a high-resolution camera with 10X zoom lens was used.

In order to ensure the reliability of the results, at least six scaffolds were tested for each geometry, three for the x direction and three for the y direction.

Through the values of Force (*F*) and Displacement (ΔL) obtained during the tensile tests, it was possible to delineate stress-strain curves for the different designs, and from these curves to remove physical quantities such as Stress (σ), Strain (Ɛ), Yield Point (σγ), Elastic Limit Strain (Ɛel), Tangent Modulus (*Et*) and Elastic Strain Energy Density (υ).

The Stress (σ),in Pascal (Pa), is determined by the equation (2), where F is in Newton (N) and A is in meters (m). The equation (3) is deducted from (Figure SI.3).

$$\sigma = \frac{F}{A} \quad 2.$$

or,

$$\sigma = \frac{F*\rho*L0}{m} \quad 3.$$

The Strain (Ɛ) is determined by the equation (4), where ΔL and *L0* are in meters (m).

$$\mathcal{E} = \frac{\Delta L}{L0} \quad 4.$$

The Tangent modulus (*Et*) is determined by the equation (5), where σ is in Pa.

$$Et = \frac{\sigma_{\sigma\gamma}}{\mathcal{E}}\ ,\ [0, \sigma\gamma] \quad 5.$$

The Elastic strain energy density (υ) is determined by the integral (6), where υ is J/m³.

$$\upsilon = \int_0^{\sigma\gamma} \frac{a}{2} * \mathcal{E}^2 + b\mathcal{E} \quad 6.$$

The Yield point (σγ) is a value in Pa that characterizes the point on the stress curve where the material ceases to have an elastic behavior. This value is obtained when the determination coefficient (R^2), of a line drawn between 10 points, starting at point 0, reaches 0.97.

3.4 GelMA Synthesis

In order to distribute the cells in the scaffolds, a GelMA hydrogel, was produced, which served as a matrix for their encapsulation.

To synthesize GelMA, gelatin powder is dissolved in a 1:10 proportion in Milli-Q water at 50 °C and with continuous stirring. When the mixture is homogeneous, methacryloyl anhydride is added dropwise with a glass pipette. After 3 hours of agitation, the supernatant (GelMA) is removed and

resuspended in Mili-Q water. A dialysis process was performed for one week on the suspension and then lyophilization, for a week, in the freeze-dryer (ZIRBUS technology, Netherlands).

3.5 MXenes Synthesis

Initially, LiF was dissolved in a concentrated HCl solution and later $TiAlC_2$ powder was added. The mixture was stirred at 45 °C for 40 hours, during which the aluminum is removed when reacting with HCl. After the etching step, the suspension was transferred to a tube and centrifuged to separate the MXenes material from the solution. The precipitate was washed repeatedly with deionized water until it reached the ideal pH.

Finally, the material was vacuum dried for 24 hours, resulting in MXenes in the form of black powder. This process was carried out by an external laboratory and the powder was diluted to a concentration of 15 % w/v.

3.5.1 Incorporating MXenes into PCL Scaffolds

Based on a recent protocol from DiedKova et al. scaffolds with side length of (ℓ) 600 µm and with an internal angle (θ) of 60 ° were incubated in MXenes solution for different periods of time. Initially, one group of structures was incubated for 90 minutes and another for 3 hours. To evaluate improved particle adhesion over time, a third test group was incubated for 24 hours [63].

Finally, in order to increase the adhesion of the particles and their uniform distribution along the fibers, another group of scaffolds was treated in an ozone atmosphere (PSD Pro Series, Digital UV Ozone System, NOVASCAN) for 15 minutes and then incubated in the MXenes solution for 3 hours [63].

3.5.2 Characterization of Scaffolds with MXenes

All previously incubated groups were analyzed by SEM (SU8220, Hitachi Regulus, Japan), allowing the qualitative evaluation of the distribution of NPs along the PCL fibers. The images acquired were obtained with 5-15 Kv under vacuum. In addition, the samples were also submitted to Energy Dispersive Spectroscopy (EDS), which is commonly coupled to SEM analysis and enables the detection of the chemical elements present, as well as their respective concentrations [70].

3.6 Biological Assays

To verify the proliferation, orientation and cell alignment, over time, in the different geometries of the scaffolds, stem cells were cultured and later seeded in hydrogel in the different hexagonal structures.

3.6.1 Cell Culture

Human mesenchymal stem cells (hMSCs) can be expanded *in vitro* as undifferentiated cells staying responsive to environmental cues. This cells were cultured in DMEM (1X).

On day 0, the cells were quickly thawed from the cryovial at 37 °C in a water bath, at either the 4th or 5th passage, and then centrifuged to remove the dimethyl sulfoxide (DMSO) to which they had been exposed. The cells were then cultured in expansion medium in a t-flask, with a cell density of 2500 cell/cm² and were incubated at 37°C with 5 % CO_2. The expansion medium was renewed every two days until the cells reach confluence.

When the cells reach confluency, the t-flask was washed twice with sterile Phosphate-Buffered Saline (PBS); cells were incubated with trypsin for 5 minutes in the incubator at 37° C with 5 % CO_2. After centrifugation, the cells were resuspended and counted on the automatic hemocytometer (Countess, Thermo Fisher Scientific) with Trypan Blue solution in the same proportion as the cell suspension; subsequently, the cells were again cultured in t-flask, with the objective of expansion.

3.6.2 Scaffold-Reinforced GelMA with Cells

Initially, the scaffolds were cut and measured to calculate a volume of hydrogel with an average value of 0.7 mm in height. In a first phase, the scaffolds were treated with sodium hydroxide (NaOH), but later this step was removed to optimize the use of microstructures.

The scaffolds, as well as the materials used for their handling, were sterilized in ethanol and under ultraviolet (UV) light inside a safety cabinet for 30 minutes. After the sterilization process, the scaffolds were washed with sterile PBS.

To prepare the hydrogel precursors, the following stock solutions were prepared: 15 % w/v of GelMA in PBS, 20 mM of Ru solution and 200 mM of SPS solution, both in PBS [71]. The combination of the use of Ru and SPS solution, as a visible light crosslinker, was later replaced by a LAP solution, as a UV light crosslinker; this stock solution has been prepared with 2 % W/V [72].

After calculating the volume needed to cover the total number of scaffolds, the required volume of GelMA and LAP were calculated to obtain a gel mixture with 5 % w/v and 0.1 % w/v, respectively. The remaining volume were filled with PBS and cell suspension. In turn, the process of trypsinization and cell counting was identical to that performed in 3.5.1; the volume of cell suspension used in PBS was calculated according to the desired cell density for each analysis (Figure 10.).

The sterile scaffolds were placed on non-stick teflon surfaces and then the gel mixture is placed on top of the microstructures in order to cover them completely. Subsequently, the scaffolds already incubated in the gel mixture are exposed to UV light for 7 to 10 minutes in order to solidify the gel

mixture (Figure 10.). The structures are placed in the incubator, at 37 °C with 5 % CO_2, in an expansion medium, which was changed every two days.

To evaluate cell proliferation and alignment in different geometries, structures with hexagonal designs with internal angles of 30 ° and 60 ° were used. For each angle, at least three structures with 400 µm and 600 µm were encased in hydrogel. In addition, for the same working groups, the use of two cell densities was tested: 20 and 25 million cells per milliliter.

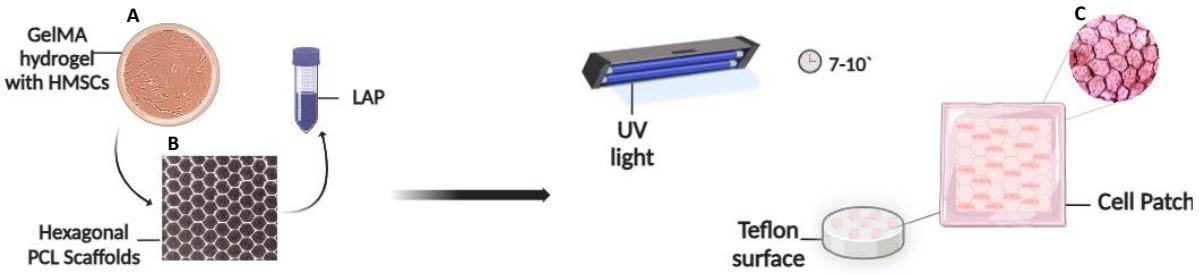

Figure 10 Encapsulation process. *Illustrative representation of the encapsulation process of the PCL scaffolds in the gel mixture with hMSCs and LAP as a crosslinker, followed by the illustration of the crosslink process by UV light under a non-adherent teflon surface element. In this representation, real images of the hMSCs culture (A) are used, of a scaffold with a hexagonal structure with an internal angle of 60 º (B) and a cell patch incubated in a crosslinked gel (C). Figure created in Biorender.*

3.6.3 PrestoBlue Assays

In order to evaluate the metabolic activity of cells of the scaffolds with hydrogel, Presto Blue Assays were performed on days 4, 6 and 10. The PrestoBlue solution was diluted in culture medium, previously heated to 37 °C, in a ratio of 1:10. In each well, 2 mL of solution is added and the well plate, protected from light by aluminum foils, is incubated for 20 minutes at 37 °C with 5 % CO_2. Then, 100 µL were taken out from each well and put on each well of 96-well plate.

The 96-well plate was put into a SYNERGY|HTX multi-mode reader (BioTek, United States) with filter wheel of 535-560 nm for the emission spectrum and 590-615 nm for the emission spectrum. Using the Systems Optics Library-Set Reader software, fluorescence was measured with an excitation/emission spectrum of 530/590 nm.

3.6.4 Fluorescent Staining

At each timepoint (days 1, 3, and 7), separate sets of patches were washed twice with PBS and then fixed with 1.5 mL of 4 % PFA at room temperature for 30 minutes. After washing the patches twice with PBS, they were permeabilized using 0.5 % Triton X-100 at RT for 30 minutes in stirring. Then, to stain the F-actin patches were emerged with a solution of phalloidin 550 (1:200) for 30 minutes in stirring at RT. To stain the DNA and allow visualization of the cell nucleus, after washing with PBS, the

patches were emerged with DAPI (1:1000) and stirring at RT for 15 minutes (Figure SI.4). Images were obtained by Confocal Laser Microscopy (TCS SP5, Leica Microsystems, Danaher, Germany) from LAS X Office software.

3.7 Statistical Analysis

All statistical analysis were performed by Anova's both, one-way and two-way with Turkey`s multiple comparisons through the GraphPad Prism software to compare the means and standard deviations between test groups. The data are considered statistically significant when probability of error (p) of $p < 0.05$. For these tests, at least three samples were used per analysis.

4. Results and Discussion

4.1 Printing Accuracy

As described in section 3.2.2, the scaffolds were printed by an additive solvent-free melted PCL deposition technique. The printing quality of MEW, due to the multi parametric and physical properties was evaluated by the fiber uniformity (printing stability) and fiber placement accuracy (printing accuracy) [73].

To fabricate the hexagonal structures, it was first necessary to ensure that the jet formed a stable Taylor Cone (Figure 11.). After stabilizing the parameters, the CTS was measured (Figure SI.7); initially, a standard rectangular pattern (Figure SI.2) with a higher speed range was defined; by using digital microscopy, the point at which the fiber began printing without colloidal movement was observed, allowing the speed gradient to be refined to a narrower range. To ensure printing stability, the transition from colloidal jet motion to a more linear motion was also identified by the curvature of the jet deposition (Figure SI.7), which became straighter when linear and stable polymer deposition was achieved (Fig 11.).

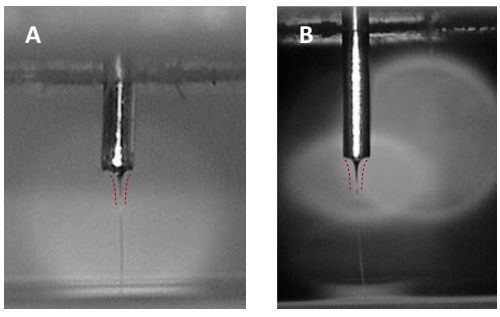

Figure 11 Printing Stability. *Images showing the molten PCL jet with a formed Taylor cone (---). (A) The initial stage of fiber extrusion, showing the jet before reaching the CTS, where a straight curvature is observed. (B) Uniform fiber deposition after achieving CTS, characterized by a linear curved jet. Images captured by a digital camera attached to the MEW printer.*

Initially, to test the different designs and printing parameters, hexagonal structures were printed with a side length of 1000 µm, at all internal angles. Figure 12 shows the difference between printing the structures without parameter optimization (A) and with the optimized printing parameters (B) between scaffolds with 35 layers and an internal angle of 60 °. In figure SI.5 images of scaffolds with 35 layers, a side length of 1000 µm and with an internal angle of 30 ° and 45 °.

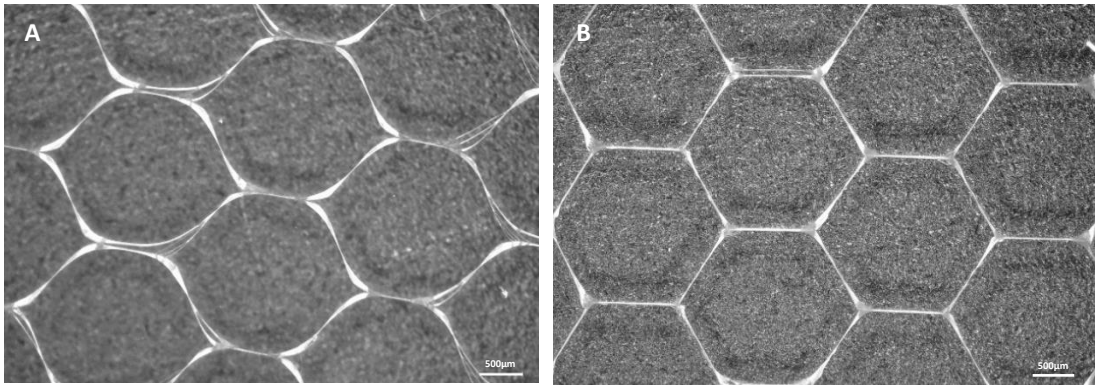

Figure 12 Scaffolds with Hexagonal Structures. *Images acquired from top perspective by digital microscopy of hexagonal meshes with a side length (ℓ) of 1000 µm with an internal angle (θ) of 60 º and 35 layers. (A) Optical image of hexagonal structures before the print parameters were optimized. (B) Image of the structures with hexagonal pattern printed with the established printing parameters: P = 1.0 bar; z = 2.50 mm; V = 3.70-4.00 Kv. Images taken from VHX software.*

Through various optimization attempts, it is clear that for microstructures that require the printing of corners with specific angles, the printing parameters are restricted. In figure 12.A it is visible a hexagonal mesh, however these are rounded at the corners due to the colloidal movement of the fiber. In turn in figure 12.B it is notorious that the parameters used are favorable to the design of a rigorous pattern, where the desired internal angles are met and where the straight fibers cross and overlap in a consistent way.

The parameters that have been defined (Table 2) were obtained by changing each of them individually followed by microscopic observation of the meshes. In general, increase some printing parameters such as the voltage and the printing speed, as well as the decrease in the pressure used and the distance from the nozzle to the collector allows the formation of more complex structures, which require the definition of precise angles at short distances. Similarly, the parameters have been optimized for the scaffolds with 35 layers, with side length of 400 µm and 600 µm, and for the three internal angles, the images are in the figure SI.6.

The geometry of a scaffold is designed to meet its applications, for example the use of smaller pore sizes that maintain their interconnectivity, aims to ensure cell proliferation and the transport flow of nutrients and metabolic waste [42]. The variables that occur during the manufacturing process can change the intended structure, so it is essential to evaluate the printing accuracy of the process (Figure 13.), in this project it was evaluated by measuring the internal angles and pore size of the scaf folds by the method described in section 3.3.1.

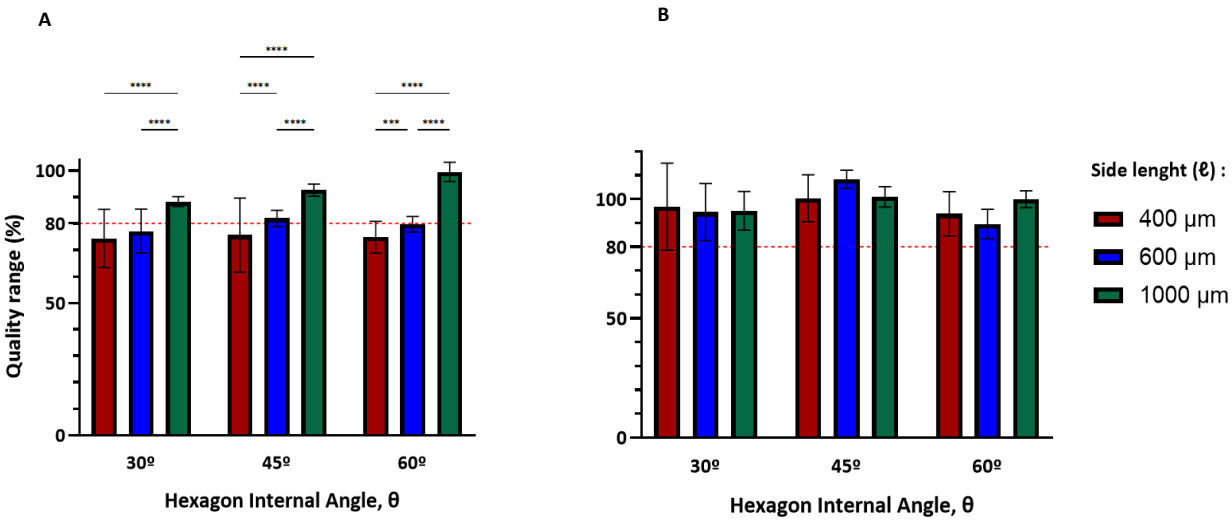

Figure 13 Printing Accuracy. *Assessment of printing accuracy (with an error margin of 20 %) of the 35-layer hexagonal structures printed with side lengths (ℓ) of 400 µm, 600 µm, and 1000 µm, and with internal angles (θ) of 30 º, 45 º, and 60 º. (A) Assess of the trajectory error through pore size measurement and comparison with the expected design size. (B) The quality range was assessed by measuring the internal angles and comparing them to the expected values, ensuring both the expected resolution and perimeter are achieved. For each analysis, at least 3 samples were used (n). (**** p< 0.0001, *** p<0.001, bars corresponding to non-significant statistics were not shown). Figure created in GraphPad Prism.*

To evaluate the printing accuracy, a margin of error of 20 % was established in relation to the expected design, in this sense, when analyzing figure 13.A, it is noticeable that the meshes with a smaller pore size (ℓ = 400 µm) are printed in a trajectory with a higher error (≈ 25 %) when compared to the meshes with the largest pore size (ℓ = 600 µm and 1000 µm). However, when we analyze figure 13.B, the similarity between the expected angles and the printed angles is confirmed. In MEW, as the pore size decreases, the precision and stability of the jet become more challenging, since the control over material deposition needs to be extremely precise [47], as confirmed by the printing accuracy of the areas in Figure 13.A. However, the printing accuracy of the internal angles does not follow the same trend of results; this difference occurs due to the horizontal movement of printing (Figure SI.8) that favors the formation of angular structures.

Due to the size of the pores and the speed needed to print them, the resolution required is hard to achieve, specifically for the structures with smaller pore size; still the analysis of both parameters for printing accuracy allows us to assess that the structures have approximately the desired hexagonal geometry, previously designed.

In this sense, it was possible to assume that the optimized printing parameters used allow the formation of scaffolds according to the intended design (Figure 9.), demonstrating a relatively high degree of similarity. However, it is still necessary for each print to check the printed structure, as well as adjust the parameters in order to obtain a higher printing accuracy.

4.2 Morphological Analysis

Regarding morphological aspects of the scaffold`s fibers, they were visualized by images taken in SEM (Figure 14.) to achieve the size of an individual fiber, the size of a 35-layer scaffolds wall and the interconnectivity of the fibers.

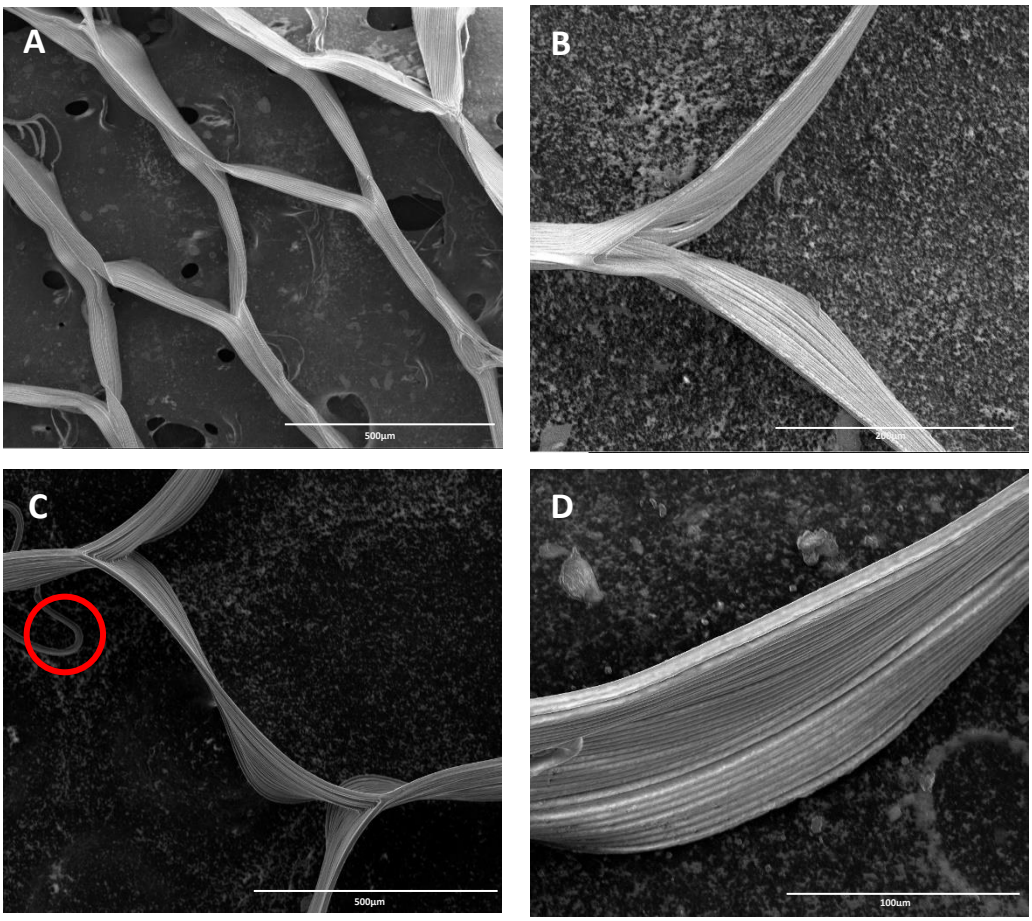

Figure 14 Morphological Analysis. *SEM images of hexagonal PCL scaffolds and fibers. (A) Hexagonal structure with an internal angle (θ) of 30 º, used to evaluate the structure and fiber interconnectivity. (B) A corner of a PCL scaffold, allowing the visualization of fiber interconnectivity and the assessment of the stacking process quality. (C) Interface between two pores of the MEW-printed microstructure, with a red highlighted single fiber confirming the connection of fibers throughout the mesh and the printed fiber dimensions. (D) A wall of 35 layers of PCL fibers, confirming the quality of the stacking process. Images were taken from the xT microscope control software.*

In tissue engineering, the porosity of a scaffolds is an insufficient factor to ensure an efficient flow of cells along the scaffold; the presence of pores facilitates the entry of cells into the structure, but the interconnectivity between them ensures that the cells are evenly distributed across the scaffold and create a three-dimensional structure [74]. MEW is a printing technology with higher control of fiber deposition comparing with other techniques such as electrospinning [45,46,47]; by using this one it was possible to fabricate precise pores with high interconnectivity.

By qualitatively analyzing the interconnectivity of the fibers, by SEM, (Figure 14. A, B and C) it is possible to confirm that the fibers connect uniformly between pores, which predicts that the cells will have a way to proliferate along them. This morphological analysis also confirmed in figure 14.C that a single fiber measures (8.4 ± 0.63) µm, just as a wall of 35 layers (Figure 14.D) measures approximately (70 ± 0.29) µm. It would be expect the wall of the scaffolds to be between 294 µm, but it turns out to be much smaller because during the polymer cooling process, as the fibers stack, they merge together [51,52]; for a more detailed analysis, the measurement in figure 14. D should have occurred perpendicular (90 °), but the difficult handling of the fibers due to their size made this analysis harder. In addition, the size of the fibers always depends on the pressure and electric field at which they are extruded [51,52] and their diameter can be increased or decreased. Also, by analyzing figures 14. B, C and D we can affirm that the stacking of the fibers is visually, stable and regular.

In cardiac tissue engineering, it is crucial that scaffolds possess a highly porous matrix, with pore sizes higher than 50 µm and high interconnectivity that ensures efficient cell migration and infiltration. Also, the interconnected porosity facilitates the diffusion of nutrients and oxygen, critical for cell survival. Additionally, these properties support the mechanical integrity of the scaffold, allowing it to mimic the native cardiac tissue's flexibility while ensuring structural stability. Moreover, high interconnectivity promotes vascularization and electrical signal propagation, both essential for the functionality of engineered cardiac tissues [42].

When evaluating the printing accuracy, which despite not fully corresponding to the measurements that were programmed, the hexagonal scaffolds manufactured by MEW obtained reasonably favorable and fairly consistent quality values, which shows a stability and reproducible capacity of the structures in all sizes of side length and with all internal angles; morphologically, the structures have highly interconnecting macropores and shows a good stacking process.

4.3 Mechanical Properties Analysis

After obtaining the manufacturing parameters of the hexagonal structures, the mechanical behavior of the scaffolds was tested by uniaxial tensile tests, with a stretching movement, in order to confirm its anisotropy, its elastic capacity, resistance and energy absorption capacity, during the elastic phase of the polymer. Figure 15 portrays a stress-strain curve of hexagonal structures, as well as the material's elongation process (in figure SI.9 the curves for structures with side lengths of 400 µm and 600 µm with internal angles of 30 ° and 60 ° are represented).

By analyzing figure 4.5, the semicrystalline and ductile structure of PCL is confirmed by the presence of the regions described in section 2.7.2.2. Initially, the toe region (A) characteristic of a deformation is visible in the x-direction without applying significant stress (this region is not visible in all curves because of the performance of an initial pre-load). Next, a linear region (B) of the curve between the stress and strain characteristic of the elastic state of the material is visible. Finally, after the yield point, the curve takes on a more planar shape (C) that identifies its plastic behavior.

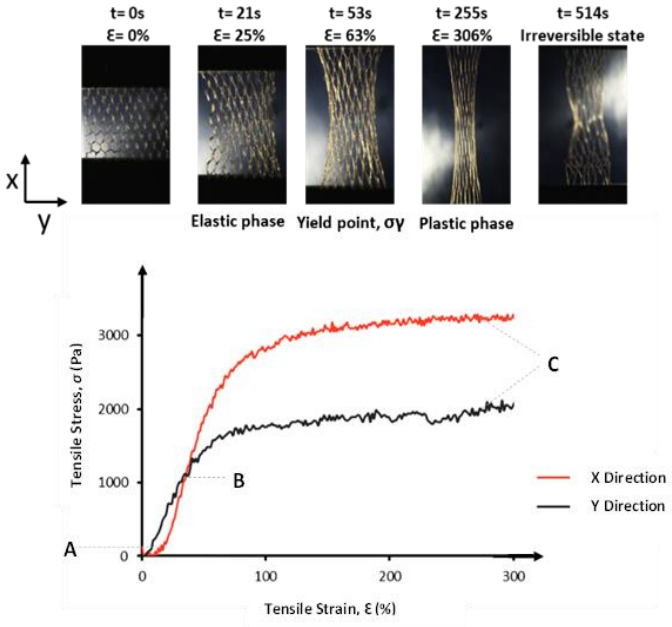

Figure 15 Mechanical Analysis (Stress-Strain Curve). *Representation of a stress-strain curve from uniaxial tensile tests of a hexagonal structure in the x-direction and y-direction, where the stress (σ) values are in Pascal (Pa) and the strain (Ɛ) values are in percentage (%) relative to the initial displacement (L0). (A) Toe region, identified by an increase in strain without the application of external forces. (B) Representation of the elastic region of a scaffold, characterized by the linear curve where displacement is proportional to the force applied to the polymer. (C) The plastic region of the curve, representing the point where the material can no longer return to its original shape. The curve was created in GraphPad Prism. Images were taken from LABJOY software.*

In addition, the difference between the behavior of the x-direction and y-direction curves in figure 15 and in figure SI.9 reveals that scaffolds have, in fact, an anisotropic structure, where the mechanical behavior of the structure varies according to the direction in which the external stress is applied.

The balance between the strength and elasticity of scaffolds are key properties in cardiac tissue engineering when trying to simulate the ECM of the cardiac muscle. These structures must have mechanical properties similar to or superior to native tissue in order to support the contraction of cardiac cycles. To assess these parameters, the yield point, elastic limit strain, tangent modulus and elastic strain energy density values were obtained by interpreting the stress-strain curves of the structures (Figure 16, 17 and 18).

The yield point and the elastic limit strain, respectively, mark the maximum point of the force that can be applied to a material and its deformation, before it enters its plastic phase. When analyzing

figure 16.A, although the last group does not have statistically significant data, it is possible to see that in all design their yield point is much higher in the x-direction compared to the y-direction due to the orientation of the print that allows greater resistance in that direction. Even though there is only statistical significance between the internal angles of the group with side length of 600 µm (in the x-direction), the data show that the yield point tends to be higher in structures with an internal angle of 30 °. In addition, it is also clear that structures with a smaller pore size (ℓ = 400 µm), tend to have a much higher yield point in the x-direction compared to scaffolds with a larger pore size.

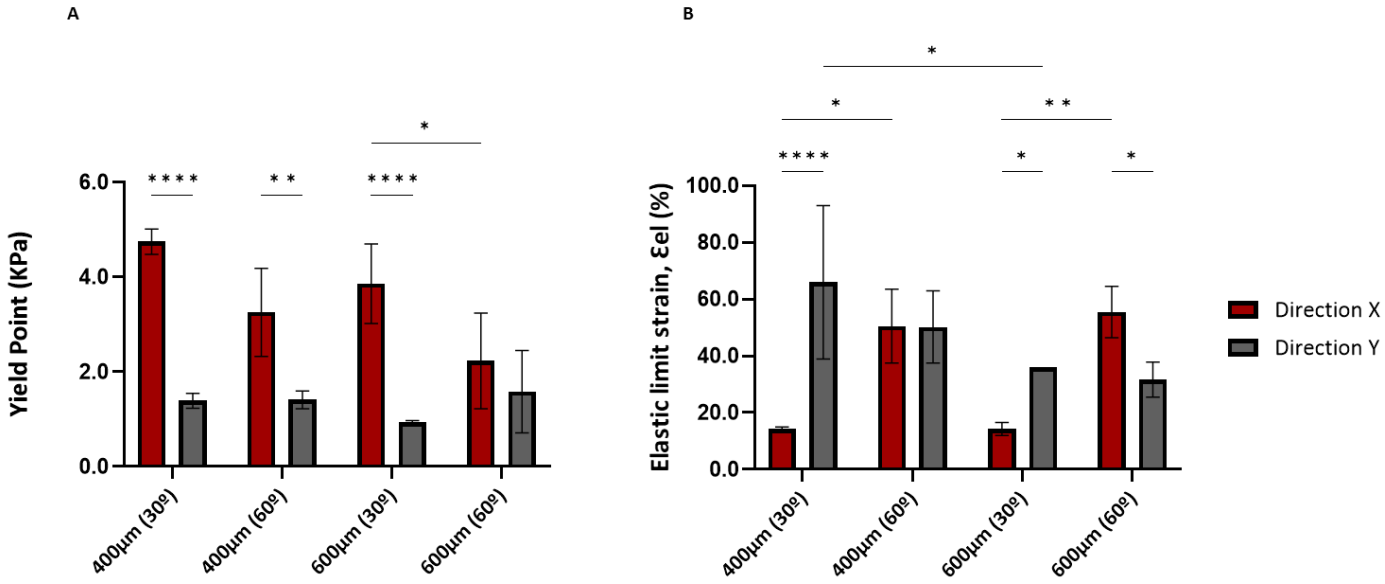

Figure 16 Mechanical Analysis (Yield Point and Elastic Limit Strain). *Mechanical analysis of hexagonal scaffolds with side lengths (ℓ) of 400 µm and 600 µm, and internal angles (θ) of 30 º and 60 º at both directions: x-direction (red) an y-direction (grey). (A) Graphical representation of the yield point values (σγ) in kilopascals (KPa). (B) Graphical representation of the elastic limit strain (Ɛel) values in percentage (%). For each analysis, at least 3 samples were used (n). (**** p< 0.0001, *** p<0.001,*p<0.05, bars corresponding to non-significant statistics were not shown). Figure created in GraphPad Prism.*

In summary, structures manufactured with a smaller pore and a lower internal angle have the ability to support superior external forces before reaching their irreversible deformation, that is, they are more resistant. In addition to the maximum force that this material is capable of withstanding, it is essential for cardiac application that the structures are able to deform in a similar or superior way to the native tissue.

The deformation capacity is obtained through the elastic limit strain, which reveals the maximum possible deformation in the elastic phase of the scaffolds. Figure 16.B shows that for groups with internal angles of 30 °, the direction y of the structures has a greater capacity to deform, however, in groups with an internal angle of 60 °, the direction with the greatest elastic limit strain is direction x. This results reveals that different designs allows differences on mechanical behaviors despite using the same material and the same printing direction. By evaluating the groups with statistical

significance, we can assess for the same pore size and on same direction, structures with higher intern angle shows a greater deformation capacity.

The stiffness of these materials can be evaluated through the modulus tangent, which directly relates the force applied to the structures with their deformation. Analyzing, figure 17 it is possible to understand that yield point and elastic limit strain are directly related to the tangent modulus.

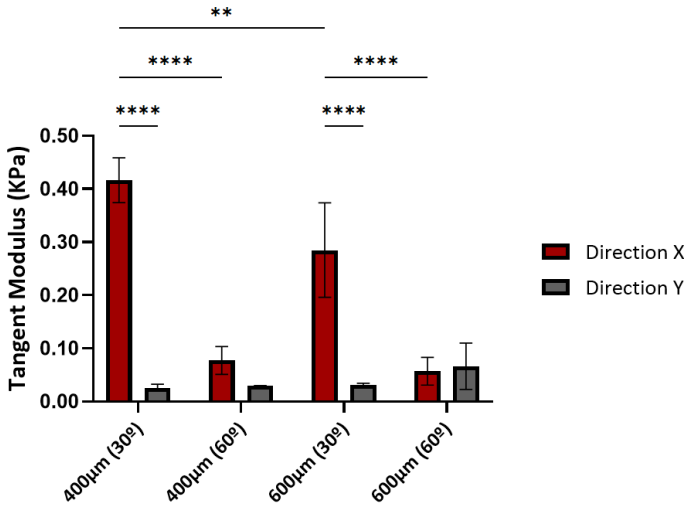

Figure 17 Mechanical Analysis (Tangent Modulus). *Mechanical analysis of hexagonal scaffolds with side lengths (ℓ) of 400 µm and 600 µm, and internal angles (θ) of 30 º and 60 º at both directions: x-direction (red) an y-direction (grey). Graphical representation of the tangent modulus values (Et) in kilopascals (KPa). For each analysis, at least 3 samples were used (n). (**** p< 0.0001,**p<0.01, bars corresponding to non-significant statistics were not shown). Figure created in GraphPad Prism.*

Although not all data are statistically significant, there is a clear tendency for structures with smaller pore size and smaller internal angle to present a higher stiffness than others. In the same way, the x-direction presents a much higher rigidity than the y-direction, in all cases except in the microstructure with a side length of 600 µm with an internal angle of 60° (values are not significant).

The modulus tangent (equation 5) is the ratio between the yield point and elastic limit strain. Despite the graphical similarity between the yield point and the tangent modulus, these are not directly proportional, as tangent modulus depends on the deformation at which the scaffolds are. Also the stiffness of the structures are defined by tangent modulus, so it demonstrates how much a material can deform up to a certain applied force.

When analyzing the three groups with statistical significance in common in figure 16 A,B and figure 17 (ℓ = 400 µm with θ of 30 °, in x and y; ℓ = 600 µm with θ of 30 °, in x and y; ℓ = 600 µm with θ of 30 ° and 60 °, in direction x). For both pore sizes, with internal angle of 30 °, the yield point is higher in the x-direction, while the Ɛel is smaller, which reflects a higher stiffness in x-direction. In turn for the same pore size (ℓ= 600 µm), in the x-direction, the yield point is higher for the design with an

internal angle of 30 ° and the Ɛel is lower, which also makes the stiffness higher. This confirms that the stiffer the material, the less deformable the scaffold will be.

Understanding the energy capacity that the material can accumulate and release in the elastic phase is also one of the crucial properties to understand the mechanical behavior of structures. This property is calculated by the area under the stress-strain curve, for integrating the trendline between zero and σγ (as described in section 3.3.3). These data can be seen in figure 18.

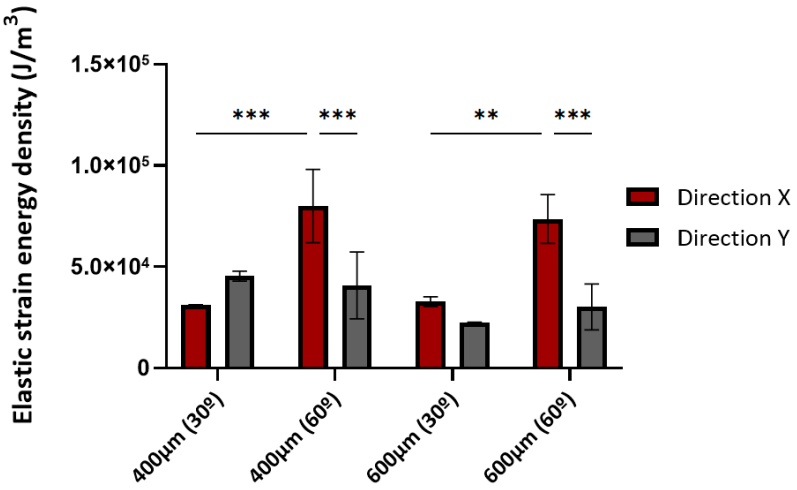

Figure 18 Mechanical Analysis (Elastic Strain Energy). *Mechanical analysis of hexagonal scaffolds with side lengths (ℓ) of 400 µm and 600 µm, and internal angles (θ) of 30 º and 60 º in both directions: x-direction (red) and y-direction (grey). Graphical representation of the elastic strain density values (υ) in joules per cubic meter (J/m³).). For each analysis, at least 3 samples were used (n). (*** p<0.001,**p<0.01, bars corresponding to non-significant statistics were not shown). Figure created in GraphPad Prism.*

The elastic energies are higher in structures with internal angles of 60 ° and in the x-direction, although the groups with internal angles of 30 ° do not have statistical significance, the values are much lower in both directions. In addition, the values are very similar when comparing pore size.

In a simplified way, hexagonal structures have greater resistance to external force (σγ) and have greater rigidity (*Et*) with smaller pores (ℓ = 400 µm), and smaller internal angles (θ = 30 °) and in the x-direction. In the x-direction, the deformation capacity is higher for structures with a smaller side length (ℓ = 400 µm) and a larger internal angle (θ = 60 °). In contrast, in the y-direction, the deformation capacity is greater when the internal angle is smaller (θ = 30 °), allowing for more flexibility in this axis. Finally, the ability to absorb energy during deformation is independent of pore size, but superior in structures with larger internal angles (θ = 60 °) and in the x-direction.

Associated with figure 15 and supplementary information 9 where the different stress-strain curves are represented, the different values between all the parameters assessed in figure 16, 17 and 18 confirm that the scaffolds had an anisotropic behavior. This difference between the directions of the

scaffolds is notorious because the x direction has a yield point and a tangent modulus superior and with a large margin of difference. These values reveal that there is an interconnectivity of the superior pores in the x-direction, being responsible for the increase of the resistance and deformation capacity of the scaffolds, producing the anisotropic effect, which thus fulfills one of the first objectives of scaffolds as structures.

As described previously, native tissue has mechanical properties that are intended to mimic, the ability of the structures to deform in relation to their initial state during the elastic phase is greater in all structures. In addition, the modulus tangent values are much lower than the cardiac tissue, which reveals that these structures are less rigid than the myocardium during its cycle, in turn the yield point is higher, in x-direction, than the lower limit of tensile strength, with the main emphasis on structures with internal angles of 30 °.

In this sense, in order to obtain scaffolds with greater resistance to tension, especially in the y-direction, without losing the anisotropic behavior, a strategy could be to increase the number of layers during manufacturing. Therefore, through MEW it was possible to print structures with a good resolution and that acquire potentially satisfactory mechanical properties, using a rigid material with a limited elastic capacity. In this sense, these structures will be used to evaluate the cellular response to these same specific designs.

4.4 Scaffold-Reinforced GelMA with Cells

In order to create a functional patch, hexagonal fiber scaffolds (ℓ = 400 µm and 600 µm; θ = 30 ° and 60 °) were combined with hMSCs (with 20 and 25M cells/ml) in GelMA hydrogel; the use of this type of cells in early stages of testing is more efficient due to its proliferative capacity and high adaptability to different microenvironments. As a positive control, only hydrogel was used in the same volume as the samples tested, maintaining the same cell density and volume.

NaOH treatment in PCL fibers is known to modify the polymer surface in order to increase biocompatibility through increased cell adhesion [75]. However, this process makes the structures more fragile and brittle, making them difficult to handle, so it was decided not to perform this treatment and only hydrate the scaffolds with PBS.

Also, initially, Ru and SPS solutions were used as a visible light crosslinker, in this process Ru works as a photocatalyst capable of chemically exciting SPS, which in turn generates free radicals [76] responsible for the formation of stable bonds with GelMA through a chemical crosslink. Despite the great biocompatibility of these crosslinkers [77], when encapsulated with the cells in the scaffold their process was time-consuming, which promoted overheating of the plates where the hydrogels were located and probably causing cell damage. In this sense, LAP was used as a chemical crosslinker, functioning itself as a photo initiator under UV light [76]. The hydrogels were then subjected to UV light for 5 to 7 minutes and then incubated in expansion medium.

After reinforcing the scaffolds with hydrogel and cells, it is relevant to assess the cell viability in interaction with the developed structures. For this experiment, the metabolic activity of the cells within the patches was monitored over time using PrestoBlue solution.

4.4.1 Cell Metabolic Activity

To measure the cell viability of hMSCs in the manufactured patches, cell metabolic activity was assessed using PrestoBlue assays as described in 3.5.3. The resazurin (non-fluorescent molecule) present in the reagent is reduced, by the cellular activity of living cells, to the red fluorescent molecule, the resorufin, that serves as an indicator of viability [78]. The relative fluorescence of the molecule can be obtained on a microplate reader; analysis that was carried out with the structures made above described in 4.4.

In these assays, cell viability of the groups with side length of 400 µm and 600 µm; and internal angles of 30 ° and 60 ° were analyzed with two cell densities, 20 and 25M cells/mL. As a positive control, the hydrogel was also subjected to the same feasibility tests, at the same time points, but only with a cell density of 20M cell/mL (Figure 19). However, these three groups were analyzed in different phases; for the group tested with 20M cells/ml (Figure 20.A) the reagent was placed directly in the wells where they were already incubated, in turn for the group with a cell density of 25M cells/ml (Figure 20.B) the patches were transferred to a sterile well in order to analyze the cells present only in the patch. In addition, this analysis is very sensitive to the incubation time of the reagent with the cells, which may contribute to the discrepancy between the relative values [79]. Thus, the analysis carried out between groups is only qualitative.

GelMA is an excellent biocompatible hydrogel [76], so it is used as a positive control, as shown in figure 19, all values are susceptible to analysis and show an increase in cellular activity over time although on day 4 and 6 the viability is very similar.

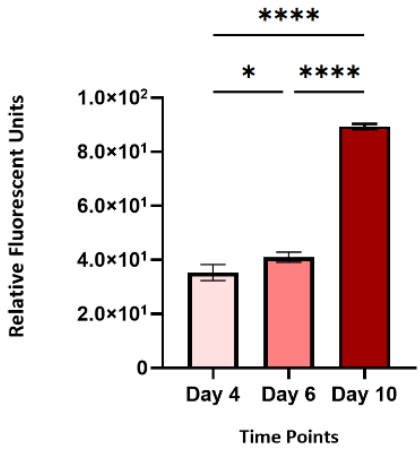

Figure 19 Cell Metabolic Activity (GelMA). *Graphical representation of cellular metabolic activity at three time points (4th, 6th, and 10th day) of GelMA hydrogel as a positive control with a cell density of 20M cells/mL. For each analysis, at least 3 samples were used (n). (**** p< 0.0001,*p<0.5). Figure created in GraphPad Prism.*

Even the values are not comparable, it is notorious that for both cell densities (Figure 20. A and B) there is a tendency for metabolic activity to increase over time. A more detailed analysis of the significant values shows that for both cell densities structures with a side length 600 µm and an internal angle of 60 ° have a higher metabolic activity when comparing with the other ones. However, due to the great intrinsic variability of these tests, their performance alone does not allow us to affirm that there is a certain design that favors cell growth. An overview, the analysis of these data shows that cell growth occurs in a similar way when compared between different cell densities and with the positive control.

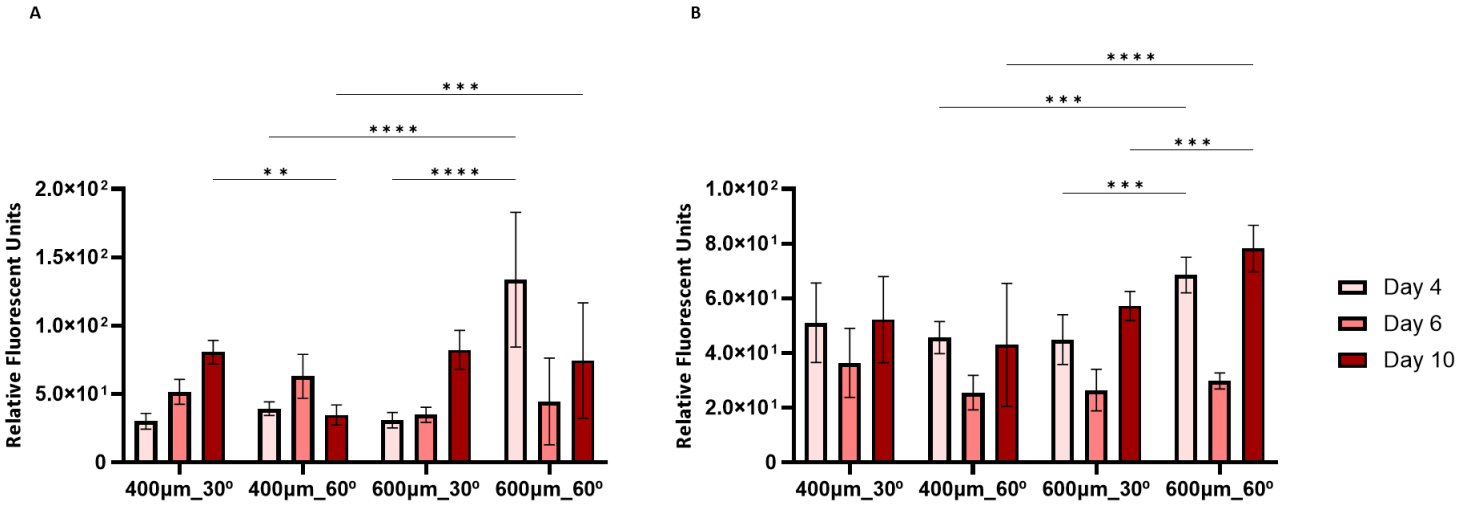

Figure 20 Cell Metabolic Activity (Cell Patches). *Graphical representation of cellular metabolic activity at three time points (4th, 6th, and 10th day) of cell patches on scaffolds with hexagonal structures, with side lengths (ℓ) of 400 µm and 600 µm, and internal angles (θ) of 30 º and 60 º, with a cell density of 20M cells/mL (A) and 25M cells/mL (B). For each analysis, at least 3 samples were used (n). (**** p< 0.0001, *** p<0.001,**p<0.01, bars corresponding to non-significant statistics were not shown). Figure created in GraphPad Prism.*

4.5 Cell Alignment Assessment

In order to evaluate the alignment of the hMSCs and their proliferation along the scaffolds, the hMSCs cell patches were labeled with DAPI (blue) and phalloidin 550 (red), which mark, respectively, the cell nuclei and F-actin (Figure 21.). Due to the lack of time available, only the group with a side length of 400 µm with an internal angle of 30 ° and 60 ° at day 7 were visualized by confocal microscopy.

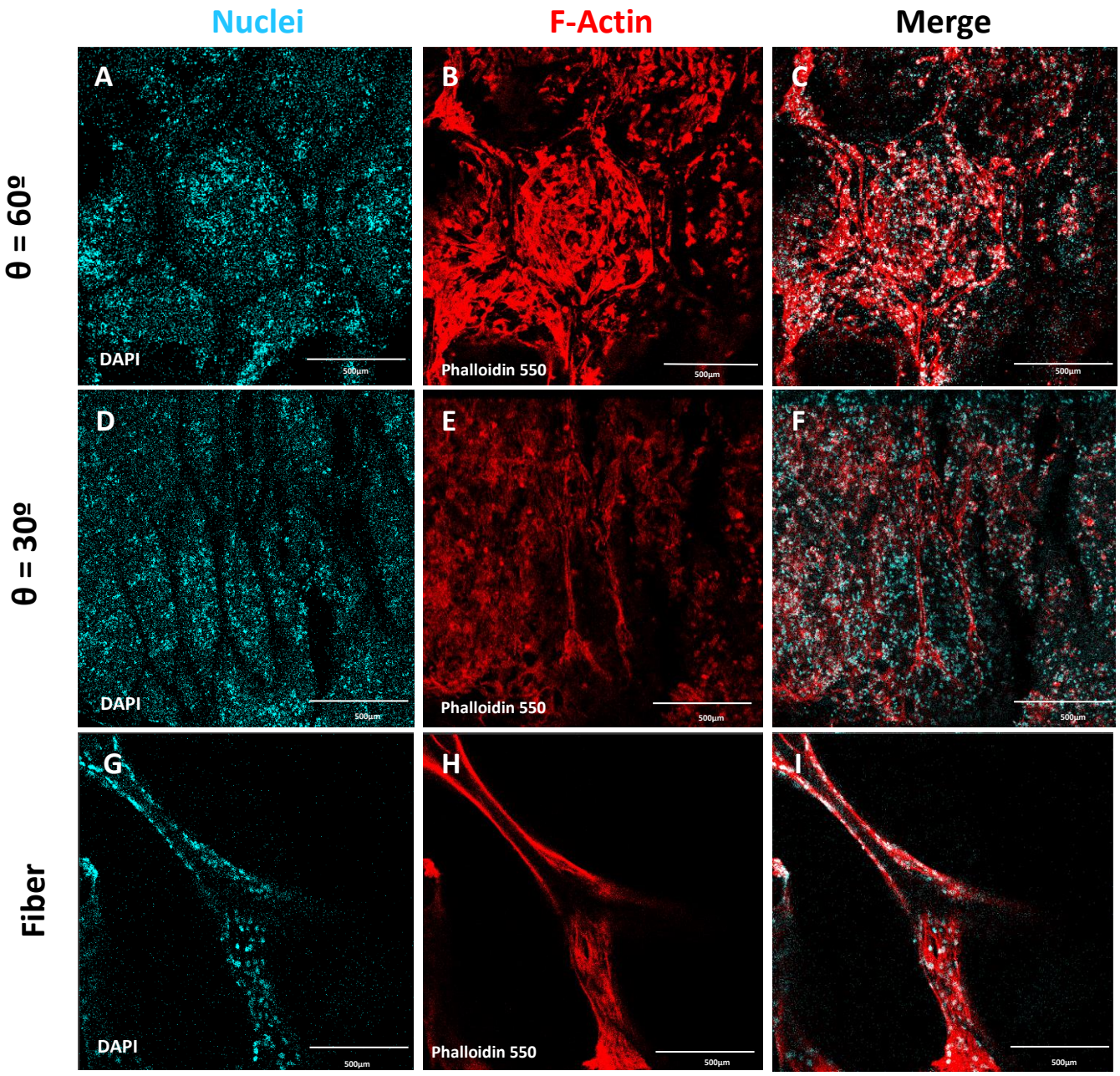

Figure 21 Nuclei and F-actin Staining. *Representative images of fluorescence confocal microscopy of cellular patches with hexagonal scaffolds at day 7 and a PCL fiber. (A) Image of cellular patches with hexagonal scaffolds with internal angle (θ) of 60 º stained with DAPI (blue). (B) Image of cellular patches with hexagonal scaffolds with internal angles (θ) of 60 º stained with phalloidin 550 (red). (C) Merged image of DAPI and phalloidin 550 staining of cellular patches with hexagonal scaffolds with internal angle (θ) of 60 º. (D) Image of cellular patches with hexagonal scaffolds with internal angle (θ) of 30 º stained with DAPI. (E) Image of cellular patches with hexagonal scaffolds with internal angles (θ) of 30 º stained with phalloidin 550. (F) Merged image of DAPI and phalloidin 550 staining of cellular patches with hexagonal scaffolds with internal angle (θ) of 30 º. (G) Image of a fiber stained with DAPI. (H) Image of a fiber stained with phalloidin 550. (I) Merged image of DAPI and phalloidin 550 staining of a fiber. Images taken from LAS X Office software.*

Figure 21 shows, for the same pore size, the difference in cell distribution and its alignment between internal angle of 60 ° (Figure 21. A,B,C) and internal angle of 30 ° (Figure 21. D,E,F). In both groups, it is possible to verify, by observation of the cell nuclei (Figure 21. A,D), that the cells are uniformly distributed in the hydrogel along the scaffolds with hexagonal structures, regardless of the design angle.

The analysis of images labeled with F-actin, a filamentous protein in the cytoskeleton of eukaryotic cells that provides structural support [80], allows for the observation of cell alignment along the fibers. In figure 21.B, it can be seen that the actin filaments are distributed across the scaffold, with greater alignment near the fibers. However, in the hexagonal structures with an internal angle of 30 °, the filaments show more uniform distribution and better alignment. Thus, scaffolds with a more elongated structure, characterized by a smaller internal angle, tend to promote enhanced cell alignment.

Finally, figure 21.G and H and I show how hMSCs effectively adhere to PCL fibers and align uniformly along them. HMSCs, in addition to their higher proliferation capacity, also have the ability to differentiate into muscle cells and cardiomyocyte strains, which makes their behavior a good indicator for future tests with CMs.

4.6 Adhesion of MXenes

Conductive NPs such as MXenes have been a new approach in the maturation of CMs, due to their ability to increase cell synchronization. The integration of these NPs into PCL fibers can be a challenge due to the weak surface interaction of the PCL and the tendency of MXenes oxidize, so different strategies were tested to understand how the NPs could adhere uniformly to them [68].

Initially, the scaffolds were incubated for two different periods of time - 90 minutes and 3 hours- with intermittent 5 minute breaks throughout the incubation period. To attempt how MXenes would integrate into the fibers, the scaffolds conductivity (both with and without silver ink at the tips of the samples) was measured but found to be zero. In order to enhance the distribution of NPs across the fibers and promote conductivity, two new strategies were designed. First, the structures were incubated in MXenes solution for 24 hours continuously, and second, a 3 hours incubation was repeated after exposing the scaffolds to an ozone atmosphere.

PCL, although mechanically favorable for tissue engineering, is an inert material, without functional groups and with low hydrophilicity [68,81]; the aim of the ozone treatment, which is simple and cost-effective, was to modify the chemical composition of the surface of the fibers to improve the adhesion of the MXenes.

Recent studies have demonstrated that ozone treatment in an aqueous environment can improve the surface properties of PCL fibers by adding functional oxygen groups, increasing their hydrophilicity while maintaining their biocompatibility properties [82]. Although this project uses an ozone atmosphere rather than an aqueous environment, similar improvements in surface properties are anticipated. Even after these two new approaches, scaffolds continued to exhibit no electrical conductivity, although visually they exhibited a darker color, which indicates the presence of MXenes. Therefore, an SEM analysis was performed on the samples to visualize the distribution of the nanoparticles after the different treatments (Figure 22) to which EDS was coupled in order to detect the presence of titanium, confirming the presence of MXenes in the structure (Figure 22 C, F, I and L).

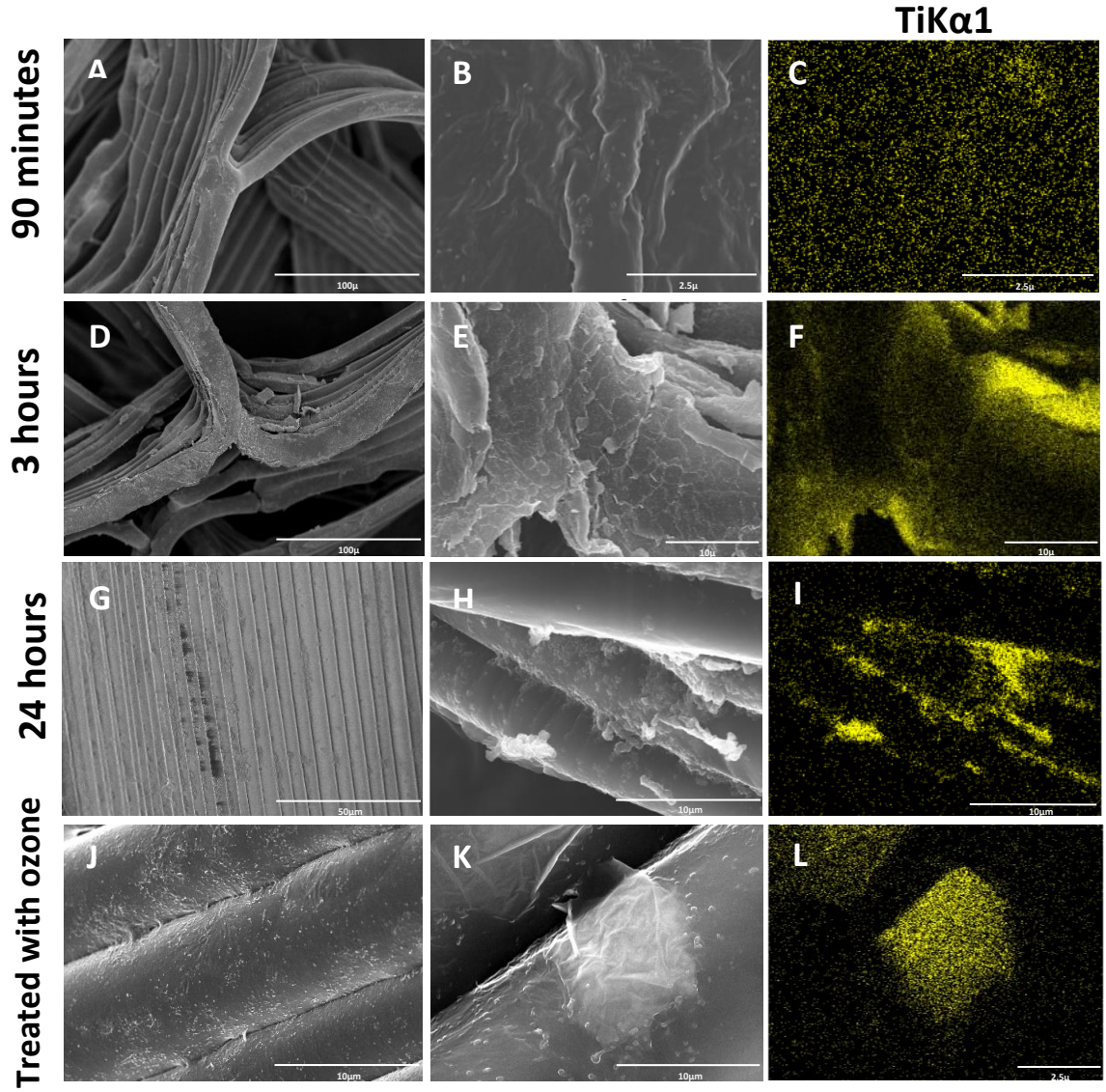

Figure 22 SEM-EDS analysis of PCL structures incubated with MXenes. *Representative images of PCL structures incubated with MXenes for different time periods and treated in an ozone atmosphere. (A) SEM image of PCL fibers incubated with MXenes for 90 minutes. (B) Magnified SEM image of PCL fibers incubated with MXenes for 90 minutes. (C) SEM-EDS image of PCL fibers incubated with MXenes for 90 minutes, showing the localized presence of titanium (TiKα1, yellow). (D) SEM image of PCL fibers incubated with MXenes for 3 hours. (E) Magnified SEM image of PCL fibers incubated with MXenes for 3 hours. (F) SEM-EDS image of PCL fibers incubated with MXenes for 3 hours, showing the localized presence of titanium (TiKα1). (G) SEM image of PCL fibers incubated with MXenes for 24 hours. (H) Magnified SEM image of PCL fibers incubated with MXenes for 24 hours. (I) SEM-EDS image of PCL fibers incubated with MXenes for 24 hours, showing the localized presence of titanium (TiKα1). (J) SEM image of PCL fibers treated with ozone and incubated with MXenes for 3 hours. (K) Magnified SEM image of PCL fibers treated with ozone and incubated with MXenes for 3 hours. (L) SEM-EDS image of PCL fibers treated with ozone and incubated with MXenes for 3 hours, showing the localized presence of titanium (TiKα1).*

The analysis of these structures was carried out in three stages for each sample. Initially, low-magnification images were captured (Figure 22 A, D, G, I), where the distribution of the NPs along the fibers can be observed. Next, the magnification was increased, allowing for images where the structure of the MXenes adhered to the fibers can be seen (Figure 22 B, E, H, K). Finally, in the previously magnified areas, EDS was performed to detect titanium (Figure 22 C, F, I, L).

The group that was incubated for a shorter period (Figure 22.A) visually shows fewer particles attached to the fibers, and the EDS analysis (Figure 22.C) indicates only a dispersion of electrons without a representative accumulation of titanium, which is confirmed by the weight percentage of 0.06 % in the sample (Figure SI.10.A). However, the groups where the samples were incubated for 3 and 24 hours show MXene accumulation and aggregation in the PCL, rather than being evenly distributed (Figure 22. D,E,G and H). The NPs accumulation, confirmed by weight percentage of 3.21% and 30% in the samples (Figure SI.10 B and C), occurs in both cases primarily at the contact points between fibers, as evidenced by the titanium signal (Figure 22. F and I). Nevertheless, the group incubated for 24 hours seems to have larger agglomerates, a result of the longer time in solution. Finally, the fibers treated with ozone exhibited a greater distribution of NPs along the entire fiber (Figure 22. J) and are arranged more uniformly (Figure 22. K); although NPs are not accumulated, they still have a high percentage of 20% (Figure SI.10 D).

In this context, it is clear that ozone treatment significantly improves the adhesion of MXenes to PCL fibers. However, it is still not sufficient to create a fully conductive fiber. Further testing is needed with a higher concentration of NPs in the solution and a longer ozone treatment of the fibers to enhance conductivity.

However, these particles are already electrically conductive by themselves and have already been proven to stimulate nerve regeneration through the transmission of neural electric signals [83], so it can be expected that their use can promote the maturation of cells that were in a process of differentiation.

5. CONCLUSION

The limited ability of cardiac cells to regenerate makes cardiovascular diseases (CVDs) a global emergency, with ischemic heart disease (IHD) being responsible for the majority of deaths. In response, tissue engineering has promoted the development of scaffolds with adjustable properties, capable of mimicking the myocardial environment.

In this master's thesis, PCL scaffolds with hexagonal structures were fabricated with side lengths of 400 µm, 600 µm, and 1000 µm, and θ of 30 °, 45 °, and 60 ° using MEW. The printing parameters for these geometries were optimized by increasing the applied voltage and decreasing the pressure and the distance from the nozzle to the collector.

The uniaxial tensile tests performed in both scaffold directions (x and y) confirmed their anisotropic behavior over time, similar to the native myocardial ECM. When mechanically characterizing the structures, the yield point values were found to be lower than the tensile strength of cardiac muscle, and the stiffness values were also significantly lower. However, for both parameters, the results remained consistent and coherent across all geometries. Thus, adjusting the scaffold size and/or fiber diameter, combined with further optimization of the printing parameters, could overcome this limitation.

In order to assess cell proliferation and alignment in the hexagonal structures, the process of encapsulating the scaffolds in GelMA with hMSCs was also optimized. Consequently, the use of NaOH was excluded, as it increased the hydrophilicity of PCL but made it more brittle. Additionally, the original crosslinker was replaced with LAP, enhancing crosslinking efficiency and increasing the likelihood of cell survival. The patches underwent preliminary viability assays, which evaluated cellular metabolic activity over time, demonstrating that the cells not only remained viable but their metabolism increased over time.

5. Conclusion

The confirmation of well-defined pores and their interconnectivity was one of the crucial parameters to assess in this project, as they are key points for cellular support and growth throughout a scaffold. This was further validated by nuclear staining with DAPI and the visualization of the cellular patches under confocal microscopy. Additionally, F-actin staining with phalloidin allowed visualization of the cellular cytoskeleton alignment along the fibers, demonstrating, as expected, more precise alignment along the fibers in structures with an internal angle of 30 °.

Finally, to enhance cellular communication, different methods of incorporating conductive materials, such as MXenes, into PCL fibers were tested. This process revealed that increasing the polymer's exposure to a nanoparticle solution promoted greater MXene agglomeration. However, a treatment that increased hydrophilicity through chemical surface modification, such as ozone atmosphere exposure, allowed for a more uniform distribution of these particles, which is more effective for the formation of conductive structures. In this sense, after an improvement in the adhesion process, the next thing will be to test cell viability with these optimized structures and understand if their maturation process is superior than with unmodified structures.

In summary, this study highlights the importance of combining biocompatible materials with geometric approaches to achieve structures with suitable properties for the development of effective scaffolds for cardiac regeneration.

FUTURE PERSPETIVES

Although this project serves as a proof of concept, there are several techniques that would be important to implement in order to achieve an effective clinical translation in future projects.

Mechanically, native cardiac tissue undergoes cyclic stretching due to the rhythmic contractions of the heart [84]. Therefore, it is a priority to perform cyclic mechanical testing on scaffolds with hexagonal structures to determine whether their mechanical properties remain effective, not only over time but throughout the cardiac cycle. This is essential for ensuring that the scaffolds can withstand the continuous mechanical stress imposed by the heart's natural function.

In this project, stem cells capable of differentiating into muscle tissue were utilized. Although the differentiation process could not be initiated, a future step in the project could involve comparing the maturation of these cells with human induced pluripotent stem cells (hiPSCs) in single culture and with the use of organoids. It is expected that organoid-based differentiation will result in superior maturation due to their ability to mimic the three-dimensional native tissue environment, which enhances cellular development [85].

Another essential analysis for cellular patches is quantitative polymerase chain reaction (qPCR), which allows for the real-time quantitative amplification of deoxyribonucleic acid (DNA) and/or RNA with high specificity [86]. This technique provides a more accurate assessment of cellular maturation and helps to better understand inherent inflammatory processes.

Finally, another essential aspect of this project with significant future potential will be testing the viability and maturation of the cells cultured with PCL scaffolds containing adhered MXenes. A key focus will be to determine whether the conductivity of these structures with NPs improves electrical communication between the cell.

REFERENCES

1. Steenman M, Lande G. Cardiac aging and heart disease in humans. *Biophys Rev*. 2017;9(2):131-137. doi:10.1007/s12551-017-0255-9
2. Cardiovascular diseases. Accessed September 22, 2024. https://www.who.int/health-topics/cardiovascular-diseases#tab=tab_1
3. The top 10 causes of death. Accessed September 22, 2024. https://www.who.int/news-room/fact-sheets/detail/the-top-10-causes-of-death
4. Castilho M, van Mil A, Maher M, et al. Melt Electrowriting Allows Tailored Microstructural and Mechanical Design of Scaffolds to Advance Functional Human Myocardial Tissue Formation. *Adv Funct Mater*. 2018;28(40):1803151. doi:10.1002/ADFM.201803151
5. Antman E, Bassand JP, Klein W, et al. Myocardial infarction redefined—a consensus document of The Joint European Society of Cardiology/American College of Cardiology committee for the redefinition of myocardial infarction: The Joint European Society of Cardiology/ American College of Cardiology Committee∗∗A list of contributors to this ESC/ACC Consensus Document is provided in Appendix B. *J Am Coll Cardiol*. 2000;36(3):959-969. doi:10.1016/S0735-1097(00)00804-4
6. Kelly RG, Buckingham ME, Moorman AF. Heart Fields and Cardiac Morphogenesis. *Cold Spring Harb Perspect Med*. 2014;4(10):a015750. doi:10.1101/CSHPERSPECT.A015750
7. Betts JGordon, Desaix Peter, Johnson Eddie, et al. Anatomy and physiology. Published online 2022:1300.
8. Takahashi K, Kakimoto Y, Toda K, Naruse K. Mechanobiology in cardiac physiology and diseases. *J Cell Mol Med*. 2013;17(2):225-232. doi:10.1111/JCMM.12027
9. Alexander Quinn T, Kohl P. Cardiac mechano-electric coupling: Acute effects of mechanical stimulation on heart rate and rhythm. *Physiol Rev*. 2021;101(1):37-92. doi:10.1152/PHYSREV.00036.2019/ASSET/IMAGES/LARGE/Z9J0042029600019.JPEG
10. Frangogiannis NG. Pathophysiology of Myocardial Infarction. *Compr Physiol*. 2015;5(4):1841-1875. doi:10.1002/CPHY.C150006
11. Tenreiro MF, Louro AF, Alves PM, Serra M. Next generation of heart regenerative therapies: progress and promise of cardiac tissue engineering. *npj Regenerative Medicine 2021 6:1*. 2021;6(1):1-17. doi:10.1038/s41536-021-00140-4
12. 54 percent of deaths in 2019 caused by cancer or CVD | CBS. Accessed September 22, 2024. https://www.cbs.nl/en-gb/news/2020/27/54-percent-of-deaths-in-2019-caused-by-cancer-or-cvd

13. Lin CJ, Lin CY, Chen CH, Zhou B, Chang CP. Partitioning the heart: mechanisms of cardiac septation and valve development. *Development*. 2012;139(18):3277-3299. doi:10.1242/DEV.063495
14. Andrés-Delgado L, Mercader N. Interplay between cardiac function and heart development. *Biochimica et Biophysica Acta (BBA) - Molecular Cell Research*. 2016;1863(7):1707-1716. doi:10.1016/J.BBAMCR.2016.03.004
15. Torrent-Guasp F, Kocica MJ, Corno AF, et al. Towards new understanding of the heart structure and function. *European Journal of Cardio-thoracic Surgery*. 2005;27(2):191-201. doi:10.1016/J.EJCTS.2004.11.026/-/DCSUPPLEMENTARIES
16. Zhang Y, Mu W, Zhang Y, et al. Recent Advances in Cardiac Patches: Materials, Preparations, and Properties. *ACS Biomater Sci Eng*. 2022;8(9):3659-3675. doi:10.1021/ACSBIOMATERIALS.2C00348/ASSET/IMAGES/LARGE/AB2C00348_0005.JPEG
17. Vunjak-Novakovic G, Tandon N, Godier A, et al. Challenges in Cardiac Tissue Engineering. *https://home.liebertpub.com/teb*. 2009;16(2):169-187. doi:10.1089/TEN.TEB.2009.0352
18. Wang L, Serpooshan V, Zhang J. Engineering Human Cardiac Muscle Patch Constructs for Prevention of Post-infarction LV Remodeling. *Front Cardiovasc Med*. 2021;8:621781. doi:10.3389/FCVM.2021.621781/BIBTEX
19. Weber KT. Cardiac interstitium in health and disease: The fibrillar collagen network. *J Am Coll Cardiol*. 1989;13(7):1637-1652. doi:10.1016/0735-1097(89)90360-4
20. Kitsuka T, Takahashi F, Reinhardt J, et al. Advances in Cardiac Tissue Engineering. *Bioengineering 2022, Vol 9, Page 696*. 2022;9(11):696. doi:10.3390/BIOENGINEERING9110696
21. Mostert D. Towards understanding the mechanisms behind structural organization of the human myocardium using human in vitro models. Published online 2024.
22. Dwyer KD, Coulombe KLK. Cardiac mechanostructure: Using mechanics and anisotropy as inspiration for developing epicardial therapies in treating myocardial infarction. *Bioact Mater*. 2021;6(7):2198-2220. doi:10.1016/J.BIOACTMAT.2020.12.015
23. Holubarsch C, Ruf T, Goldstein DJ, et al. Existence of the Frank-Starling mechanism in the failing human heart: Investigations on the organ, tissue, and sarcomere levels. *Circulation*. 1996;94(4):683-689. doi:10.1161/01.CIR.94.4.683/ASSET/3E3602DE-139D-4EB5-996C-8C1BFAB17A3D/ASSETS/GRAPHIC/0030F8.JPEG
24. del Monte-Nieto G, Fischer JW, Gorski DJ, Harvey RP, Kovacic JC. Basic Biology of Extracellular Matrix in the Cardiovascular System, Part 1/4: JACC Focus Seminar. *J Am Coll Cardiol*. 2020;75(17):2169-2188. doi:10.1016/J.JACC.2020.03.024
25. Santos ARMP, Jang Y, Son I, Kim J, Park Y. Recapitulating Cardiac Structure and Function In Vitro from Simple to Complex Engineering. *Micromachines 2021, Vol 12, Page 386*. 2021;12(4):386. doi:10.3390/MI12040386
26. Liu Z, Zhang Z, Ritchie RO. Structural Orientation and Anisotropy in Biological Materials: Functional Designs and Mechanics. *Adv Funct Mater*. 2020;30(10). doi:10.1002/ADFM.201908121

27. Ghonim S, Voges I, Gatehouse PD, et al. Myocardial Architecture, Mechanics, and Fibrosis in Congenital Heart Disease. *Front Cardiovasc Med*. 2017;4:258682. doi:10.3389/FCVM.2017.00030/BIBTEX
28. Sommer G, Schriefl AJ, Andrä M, et al. Biomechanical properties and microstructure of human ventricular myocardium. *Acta Biomater*. 2015;24:172-192. doi:10.1016/J.ACTBIO.2015.06.031
29. Falk E. Pathogenesis of Atherosclerosis. *J Am Coll Cardiol*. 2006;47(8 SUPPL.). doi:10.1016/J.JACC.2005.09.068
30. Almeida H V., Tenreiro MF, Louro AF, et al. Human Extracellular-Matrix Functionalization of 3D hiPSC-Based Cardiac Tissues Improves Cardiomyocyte Maturation. *ACS Appl Bio Mater*. 2021;4(2):1888-1899. doi:10.1021/ACSABM.0C01490/ASSET/IMAGES/LARGE/MT0C01490_0004.JPEG
31. Curtis MW, Russell B. Cardiac Tissue Engineering. *Journal of Cardiovascular Nursing*. 2009;24(2):87-92. doi:10.1097/01.JCN.0000343562.06614.49
32. Eschenhagen T, Zimmermann WH. Engineering myocardial tissue. *Circ Res*. 2005;97(12):1220-1231. doi:10.1161/01.RES.0000196562.73231.7D/ASSET/632BC3F3-6BE7-4BDD-8C5B-D7BAD24B038D/ASSETS/GRAPHIC/5FF2.JPEG
33. Taylor DA, Atkins BZ, Hungspreugs P, et al. Regenerating functional myocardium: Improved performance after skeletal myoblast transplantation. *Nature Medicine 1998 4:8*. 1998;4(8):929-933. doi:10.1038/nm0898-929
34. Reinecke H, MacDonald GH, Hauschka SD, Murry CE. Electromechanical Coupling between Skeletal and Cardiac MuscleImplications for Infarct Repair. *Journal of Cell Biology*. 2000;149(3):731-740. doi:10.1083/JCB.149.3.731
35. Chien KR, Frisén J, Fritsche-Danielson R, Melton DA, Murry CE, Weissman IL. Regenerating the field of cardiovascular cell therapy. *Nature Biotechnology 2019 37:3*. 2019;37(3):232-237. doi:10.1038/s41587-019-0042-1
36. Hatzistergos KE, Vedenko A. Cardiac Cell Therapy 3.0: The Beginning of the End or the End of the Beginning? *Circ Res*. 2017;121(2):95-97. doi:10.1161/CIRCRESAHA.117.311293/ASSET/C5CB491A-2A52-410C-B854-BDBA52EE7A55/ASSETS/GRAPHIC/95FIG01.JPEG
37. Li M, Wu H, Yuan Y, Hu B, Gu N. Recent fabrications and applications of cardiac patch in myocardial infarction treatment. *View*. 2022;3(2):20200153. doi:10.1002/VIW.20200153
38. Hutmacher DW, Sittinger M, Risbud M V. Scaffold-based tissue engineering: Rationale for computer-aided design and solid free-form fabrication systems. *Trends Biotechnol*. 2004;22(7):354-362. doi:10.1016/J.TIBTECH.2004.05.005/ASSET/BC6B4675-3E79-46A6-84F0-B450A1789885/MAIN.ASSETS/GR4.SML
39. Henkel J, Hutmacher DW. Design and fabrication of scaffold-based tissue engineering. *BioNanoMaterials*. 2013;14(3-4):171-193. doi:10.1515/BNM-2013-0021/XML

40. Hollister SJ. Scaffold Design and Manufacturing: From Concept to Clinic. *Advanced Materials*. 2009;21(32-33):3330-3342. doi:10.1002/ADMA.200802977
41. Loh QL, Choong C. Three-Dimensional Scaffolds for Tissue Engineering Applications: Role of Porosity and Pore Size. *https://home.liebertpub.com/teb*. 2013;19(6):485-502. doi:10.1089/TEN.TEB.2012.0437
42. Weigel T, Schinkel G, Lendlein A. Design and preparation of polymeric scaffolds for tissue engineering. *Expert Rev Med Devices*. 2006;3(6):835-851. doi:10.1586/17434440.3.6.835
43. Mohammed A, Abdullah A. SCANNING ELECTRON MICROSCOPY (SEM): A REVIEW.
44. Goldstein JI, Newbury DE, Echlin P, et al. Special Topics in Scanning Electron Microscopy. *Scanning Electron Microscopy and X-ray Microanalysis*. Published online 2003:195-270. doi:10.1007/978-1-4615-0215-9_5
45. Murphy S V., Atala A. 3D bioprinting of tissues and organs. *Nature Biotechnology 2014 32:8*. 2014;32(8):773-785. doi:10.1038/nbt.2958
46. Bajaj P, Schweller RM, Khademhosseini A, West JL, Bashir R. 3D biofabrication strategies for tissue engineering and regenerative medicine. *Annu Rev Biomed Eng*. 2014;16(Volume 16, 2014):247-276. doi:10.1146/ANNUREV-BIOENG-071813-105155/CITE/REFWORKS
47. Van Blitterswijk CA, De Boer J. Tissue Engineering. *Tissue Engineering: Second Edition*. Published online December 10, 2015:1-858. doi:10.1016/C2013-0-00564-6
48. Billiet T, Vandenhaute M, Schelfhout J, Van Vlierberghe S, Dubruel P. A review of trends and limitations in hydrogel-rapid prototyping for tissue engineering. *Biomaterials*. 2012;33(26):6020-6041. doi:10.1016/J.BIOMATERIALS.2012.04.050
49. Fridrikh S V., Yu JH, Brenner MP, Rutledge GC. Controlling the Fiber Diameter during Electrospinning. *Phys Rev Lett*. 2003;90(14):4. doi:10.1103/PHYSREVLETT.90.144502/FIGURES/4/MEDIUM
50. Brown TD, Dalton PD, Hutmacher DW. Direct writing by way of melt electrospinning. *Adv Mater*. 2011;23(47):5651-5657. doi:10.1002/ADMA.201103482
51. Dalton PD. Melt electrowriting with additive manufacturing principles. *Curr Opin Biomed Eng*. 2017;2:49-57. doi:10.1016/J.COBME.2017.05.007
52. Loewner S, Heene S, Baroth T, et al. Recent advances in melt electro writing for tissue engineering for 3D printing of microporous scaffolds for tissue engineering. *Front Bioeng Biotechnol*. 2022;10:896719. doi:10.3389/FBIOE.2022.896719/BIBTEX
53. Mieszczanek P, Robinson TM, Dalton PD, et al. Convergence of Machine Vision and Melt Electrowriting. *Advanced Materials*. 2021;33(29):2100519. doi:10.1002/ADMA.202100519
54. Lamprou DA, Sebe I, Éva Uhljar L, Ambrus R. Electrospinning of Potential Medical Devices (Wound Dressings, Tissue Engineering Scaffolds, Face Masks) and Their Regulatory Approach. *Pharmaceutics 2023, Vol 15, Page 417*. 2023;15(2):417. doi:10.3390/PHARMACEUTICS15020417

55. Kade JC, Dalton PD. Polymers for Melt Electrowriting. *Adv Healthc Mater*. 2021;10(1):2001232. doi:10.1002/ADHM.202001232
56. Woodruff MA, Hutmacher DW. The return of a forgotten polymer—Polycaprolactone in the 21st century. *Prog Polym Sci*. 2010;35(10):1217-1256. doi:10.1016/J.PROGPOLYMSCI.2010.04.002
57. Devlin BL, Allenby MC, Ren J, et al. Materials Design Innovations in Optimizing Cellular Behavior on Melt Electrowritten (MEW) Scaffolds. *Adv Funct Mater*. 2024;34(18):2313092. doi:10.1002/ADFM.202313092
58. Löblein J, Lorson T, Komma M, et al. An initiator- and catalyst-free hydrogel coating process for 3D printed medical-grade poly(ε-caprolactone). *Beilstein Journal of Organic Chemistry 17:136*. 2021;17(1):2095-2101. doi:10.3762/BJOC.17.136
59. Van De Velde K, Kiekens P. Biopolymers: overview of several properties and consequences on their applications. *Polym Test*. 2002;21(4):433-442. doi:10.1016/S0142-9418(01)00107-6
60. Ruan JL, Tulloch NL, Razumova M V., et al. Mechanical Stress Conditioning and Electrical Stimulation Promote Contractility and Force Maturation of Induced Pluripotent Stem Cell-Derived Human Cardiac Tissue. *Circulation*. 2016;134(20):1557-1567. doi:10.1161/CIRCULATIONAHA.114.014998/SUPPL_FILE/CIRC_CIRCULATIONAHA-2014-014998_SUPP1_EDITED20161027.PDF
61. Young RJ, Lovell PA. INTRODUCTION TO POLYMERS, Third Edition. *Introduction to Polymers, Third Edition*. Published online January 1, 2011:1-653. doi:10.1201/9781439894156/INTRODUCTION-POLYMERS-ROBERT-YOUNG-PETER-LOVELL
62. Siviour CR, Jordan JL. High Strain Rate Mechanics of Polymers: A Review. *Journal of Dynamic Behavior of Materials 2016 2:1*. 2016;2(1):15-32. doi:10.1007/S40870-016-0052-8
63. Diedkova K, Husak Y, Simka W, et al. Novel electrically conductive electrospun PCL-MXene scaffolds for cardiac tissue regeneration. *Graphene and 2D Materials 2023 9:1*. 2023;9(1):59-76. doi:10.1007/S41127-023-00071-5
64. Nekounam H, Gholizadeh S, Allahyari Z, et al. Electroconductive scaffolds for tissue regeneration: Current opportunities, pitfalls, and potential solutions. *Mater Res Bull*. 2021;134:111083. doi:10.1016/J.MATERRESBULL.2020.111083
65. Baei P, Hosseini M, Baharvand H, Pahlavan S. Electrically conductive materials for in vitro cardiac microtissue engineering. *J Biomed Mater Res A*. 2020;108(5):1203-1213. doi:10.1002/JBM.A.36894
66. Orza A, Soritau O, Olenic L, et al. Electrically conductive gold-coated collagen nanofibers for placental-derived mesenchymal stem cells enhanced differentiation and proliferation. *ACS Nano*. 2011;5(6):4490-4503. doi:10.1021/NN1035312/SUPPL_FILE/NN1035312_SI_001.PDF
67. Edwards SL, Werkmeister JA, Ramshaw JAM. Carbon nanotubes in scaffolds for tissue engineering. *Expert Rev Med Devices*. 2009;6(5):499-505. doi:10.1586/ERD.09.29

68. Basara G, Saeidi-Javash M, Ren X, et al. Electrically conductive 3D printed Ti3C2Tx MXene-PEG composite constructs for cardiac tissue engineering. *Acta Biomater*. 2022;139:179-189. doi:10.1016/J.ACTBIO.2020.12.033
69. Anasori B, Naguib M. Two-dimensional MXenes. *MRS Bull*. 2023;48(3):238-244. doi:10.1557/S43577-023-00500-Z/FIGURES/3
70. Kahouli M, Barhoumi A, Bouzid A, Al-Hajry A, Guermazi S. Structural and optical properties of ZnO nanoparticles prepared by direct precipitation method. *Superlattices Microstruct*. 2015;85:7-23. doi:10.1016/J.SPMI.2015.05.007
71. Paul S, Schrobback K, Tran A, et al. Photo-Cross-Linkable, Injectable, and Highly Adhesive GelMA-Glycol Chitosan Hydrogels for Cartilage Repair. *Adv Healthc Mater*. 2023;12(32):2302078. doi:10.1002/ADHM.202302078
72. Pilavci E, Ayran M, Ulubay D, et al. Fabrication and characterization of electrospun GelMA/PCL/CS nanofiber composites for wound dressing applications. *J Bioact Compat Polym*. 2023;38(1):3-24. doi:10.1177/08839115221138777/ASSET/IMAGES/LARGE/10.1177_08839115221138777-FIG10.JPEG
73. Cao K, Zhang F, Zaeri A, et al. Advances in design and quality of melt electrowritten scaffolds. *Mater Des*. 2023;226:111618. doi:10.1016/J.MATDES.2023.111618
74. Miot S, Woodfield T, Daniels AU, et al. Effects of scaffold composition and architecture on human nasal chondrocyte redifferentiation and cartilaginous matrix deposition. *Biomaterials*. 2005;26(15):2479-2489. doi:10.1016/J.BIOMATERIALS.2004.06.048
75. Serrano MC, Pagani R, Ameer GA, Vallet-Regí M, Portolés MT. Endothelial cells derived from circulating progenitors as an effective source to functional endothelialization of NaOH-treated poly(ε-caprolactone) films. *J Biomed Mater Res A*. 2008;87A(4):964-971. doi:10.1002/JBM.A.31728
76. Sun A, He X, Ji X, et al. Current research progress of photopolymerized hydrogels in tissue engineering. *Chinese Chemical Letters*. 2021;32(7):2117-2126. doi:10.1016/J.CCLET.2021.01.048
77. Lim KS, Schon BS, Mekhileri N V., et al. New Visible-Light Photoinitiating System for Improved Print Fidelity in Gelatin-Based Bioinks. *ACS Biomater Sci Eng*. 2016;2(10):1752-1762. doi:10.1021/ACSBIOMATERIALS.6B00149/ASSET/IMAGES/LARGE/AB-2016-001498_0010.JPEG
78. Lall N, Henley-Smith CJ, De Canha MN, Oosthuizen CB, Berrington D. Viability Reagent, PrestoBlue, in Comparison with Other Available Reagents, Utilized in Cytotoxicity and Antimicrobial Assays. *Int J Microbiol*. 2013;2013(1):420601. doi:10.1155/2013/420601
79. Yue K, Trujillo-de Santiago G, Alvarez MM, Tamayol A, Annabi N, Khademhosseini A. Synthesis, properties, and biomedical applications of gelatin methacryloyl (GelMA) hydrogels. *Biomaterials*. 2015;73:254-271. doi:10.1016/J.BIOMATERIALS.2015.08.045

80. Wulf E, Deboben A, Bautz FA, Faulstich H, Wieland T. Fluorescent phallotoxin, a tool for the visualization of cellular actin. *Proceedings of the National Academy of Sciences*. 1979;76(9):4498-4502. doi:10.1073/PNAS.76.9.4498
81. Ahadian S, Khademhosseini A. Smart scaffolds in tissue regeneration. *Regen Biomater*. 2018;5(3):125-128. doi:10.1093/RB/RBY007
82. Dabasinskaite L, Krugly E, Baniukaitiene O, et al. The Effect of Ozone Treatment on the Physicochemical Properties and Biocompatibility of Electrospun Poly(ε)caprolactone Scaffolds. *Pharmaceutics 2021, Vol 13, Page 1288*. 2021;13(8):1288. doi:10.3390/PHARMACEUTICS13081288
83. Nan LP, Lin Z, Wang F, et al. Ti3C2Tx MXene-Coated Electrospun PCL Conduits for Enhancing Neurite Regeneration and Angiogenesis. *Front Bioeng Biotechnol*. 2022;10:850650. doi:10.3389/FBIOE.2022.850650/BIBTEX
84. Zhao G, Bao X, Huang G, Xu F, Zhang X. Differential Effects of Directional Cyclic Stretching on the Functionalities of Engineered Cardiac Tissues. *ACS Appl Bio Mater*. 2019;2(8):3508-3519. doi:10.1021/ACSABM.9B00414/ASSET/IMAGES/LARGE/MT-2019-004148_0008.JPEG
85. Lewis-Israeli YR, Wasserman AH, Aguirre A. Heart Organoids and Engineered Heart Tissues: Novel Tools for Modeling Human Cardiac Biology and Disease. *Biomolecules 2021, Vol 11, Page 1277*. 2021;11(9):1277. doi:10.3390/BIOM11091277
86. Postollec F, Falentin H, Pavan S, Combrisson J, Sohier D. Recent advances in quantitative PCR (qPCR) applications in food microbiology. *Food Microbiol*. 2011;28(5):848-861. doi:10.1016/J.FM.2011.02.008

APPENDIX

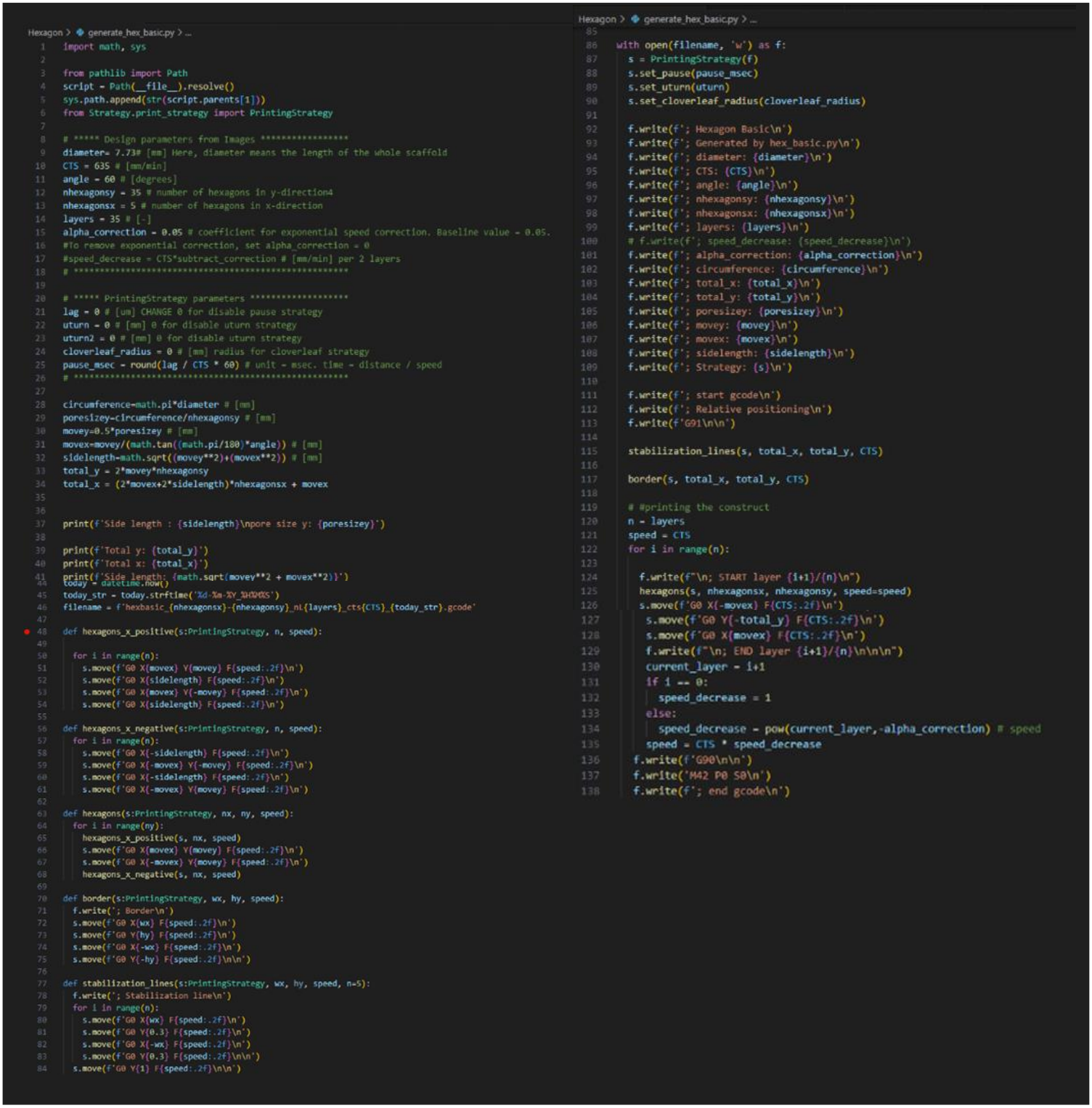

```python
import math, sys

from pathlib import Path
script = Path(__file__).resolve()
sys.path.append(str(script.parents[1]))
from Strategy.print_strategy import PrintingStrategy

# ***** Design parameters from Images *****************
diameter= 7.73# [mm] Here, diameter means the length of the whole scaffold
CTS = 635 # [mm/min]
angle = 60 # [degrees]
nhexagonsy = 35 # number of hexagons in y-direction4
nhexagonsx = 5 # number of hexagons in x-direction
layers = 35 # [-]
alpha_correction = 0.05 # coefficient for exponential speed correction. Baseline value = 0.05.
#To remove exponential correction, set alpha_correction = 0
#speed_decrease = CTS*subtract_correction # [mm/min] per 2 layers
# ************************************************

# ***** PrintingStrategy parameters ******************
lag = 0 # [um] CHANGE 0 for disable pause strategy
uturn = 0 # [mm] 0 for disable uturn strategy
uturn2 = 0 # [mm] 0 for disable uturn strategy
cloverleaf_radius = 0 # [mm] radius for cloverleaf strategy
pause_msec = round(lag / CTS * 60) # unit = msec. time = distance / speed
# ************************************************

circumference=math.pi*diameter # [mm]
poresizey=circumference/nhexagonsy # [mm]
movey=0.5*poresizey # [mm]
movex=movey/(math.tan((math.pi/180)*angle)) # [mm]
sidelength=math.sqrt((movey**2)+(movex**2)) # [mm]
total_y = 2*movey*nhexagonsy
total_x = (2*movex+2*sidelength)*nhexagonsx + movex


print(f'Side length : {sidelength}\npore size y: {poresizey}')

print(f'Total y: {total_y}')
print(f'Total x: {total_x}')
print(f'Side length: {math.sqrt(movey**2 + movex**2)}')
today = datetime.now()
today_str = today.strftime('%d-%m-%Y_%H%M%S')
filename = f'hexbasic_{nhexagonsx}-{nhexagonsy}_n{layers}_cts{CTS}_{today_str}.gcode'

def hexagons_x_positive(s:PrintingStrategy, n, speed):

  for i in range(n):
    s.move(f'G0 X{movex} Y{movey} F{speed:.2f}\n')
    s.move(f'G0 X{sidelength} F{speed:.2f}\n')
    s.move(f'G0 X{movex} Y{-movey} F{speed:.2f}\n')
    s.move(f'G0 X{sidelength} F{speed:.2f}\n')

def hexagons_x_negative(s:PrintingStrategy, n, speed):
  for i in range(n):
    s.move(f'G0 X{-sidelength} F{speed:.2f}\n')
    s.move(f'G0 X{-movex} Y{-movey} F{speed:.2f}\n')
    s.move(f'G0 X{-sidelength} F{speed:.2f}\n')
    s.move(f'G0 X{-movex} Y{movey} F{speed:.2f}\n')

def hexagons(s:PrintingStrategy, nx, ny, speed):
  for i in range(ny):
    hexagons_x_positive(s, nx, speed)
    s.move(f'G0 X{movex} Y{movey} F{speed:.2f}\n')
    s.move(f'G0 X{-movex} Y{movey} F{speed:.2f}\n')
    hexagons_x_negative(s, nx, speed)

def border(s:PrintingStrategy, wx, hy, speed):
  f.write('; Border\n')
  s.move(f'G0 X{wx} F{speed:.2f}\n')
  s.move(f'G0 Y{hy} F{speed:.2f}\n')
  s.move(f'G0 X{-wx} F{speed:.2f}\n')
  s.move(f'G0 Y{-hy} F{speed:.2f}\n\n')

def stabilization_lines(s:PrintingStrategy, wx, hy, speed, n=5):
  f.write('; Stabilization line\n')
  for i in range(n):
    s.move(f'G0 X{wx} F{speed:.2f}\n')
    s.move(f'G0 Y{0.3} F{speed:.2f}\n')
    s.move(f'G0 X{-wx} F{speed:.2f}\n')
    s.move(f'G0 Y{0.3} F{speed:.2f}\n\n')
  s.move(f'G0 Y{1} F{speed:.2f}\n\n')
```

```python
with open(filename, 'w') as f:
  s = PrintingStrategy(f)
  s.set_pause(pause_msec)
  s.set_uturn(uturn)
  s.set_cloverleaf_radius(cloverleaf_radius)

  f.write(f'; Hexagon Basic\n')
  f.write(f'; Generated by hex_basic.py\n')
  f.write(f'; diameter: {diameter}\n')
  f.write(f'; CTS: {CTS}\n')
  f.write(f'; angle: {angle}\n')
  f.write(f'; nhexagonsy: {nhexagonsy}\n')
  f.write(f'; nhexagonsx: {nhexagonsx}\n')
  f.write(f'; layers: {layers}\n')
  # f.write(f'; speed_decrease: {speed_decrease}\n')
  f.write(f'; alpha_correction: {alpha_correction}\n')
  f.write(f'; circumference: {circumference}\n')
  f.write(f'; total_x: {total_x}\n')
  f.write(f'; total_y: {total_y}\n')
  f.write(f'; poresizey: {poresizey}\n')
  f.write(f'; movey: {movey}\n')
  f.write(f'; movex: {movex}\n')
  f.write(f'; sidelength: {sidelength}\n')
  f.write(f'; Strategy: {s}\n')

  f.write(f'; start gcode\n')
  f.write(f'; Relative positioning\n')
  f.write(f'G91\n\n')

  stabilization_lines(s, total_x, total_y, CTS)

  border(s, total_x, total_y, CTS)

  # #printing the construct
  n = layers
  speed = CTS
  for i in range(n):

    f.write(f"\n; START layer {i+1}/{n}\n")
    hexagons(s, nhexagonsx, nhexagonsy, speed=speed)
    s.move(f'G0 X{-movex} F{CTS:.2f}\n')
    s.move(f'G0 Y{-total_y} F{CTS:.2f}\n')
    s.move(f'G0 X{movex} F{CTS:.2f}\n')
    f.write(f"\n; END layer {i+1}/{n}\n\n\n")
    current_layer = i+1
    if i == 0:
      speed_decrease = 1
    else:
      speed_decrease = pow(current_layer,-alpha_correction) # speed
    speed = CTS * speed_decrease
  f.write(f'G90\n\n')
  f.write('M42 P0 S0\n')
  f.write(f'; end gcode\n')
```

Figure SI 1. *Python Script for generating G-code to define the hexagonal structure for printing. Image taken from Visual Studio Code.*

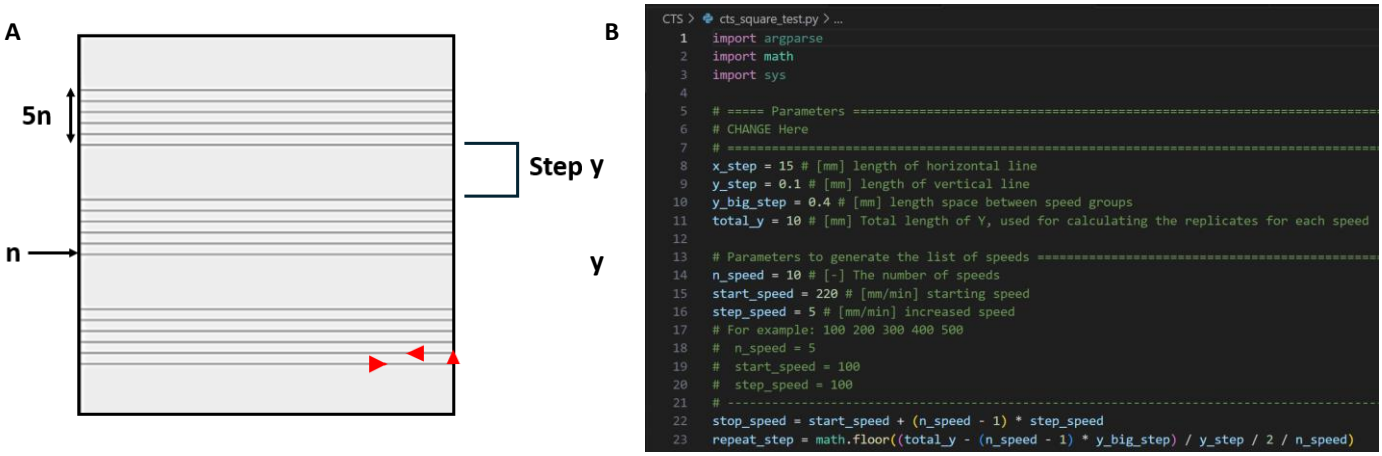

Figure SI 2. *(A) Representation of a velocity pattern that allows the CTS to be established. The red arrows are a schematic illustration of the parallel direction in which the fiber is deposed;* ***n*** *represents a fiber with a specific speed that is printed five times before changing to another defined speed, which occurs after step y. Figure taken from NCViewer. (B) Python Script for generating G-code to define the CTS pattern. Image taken from Visual Studio Code.*

$$\sigma = \frac{F}{A} \leftrightarrow A = \frac{F}{\sigma} \leftrightarrow \frac{V}{L0} = \frac{F}{\sigma} \leftrightarrow \frac{m}{\rho} = \frac{F * L0}{\sigma} \leftrightarrow \sigma = \frac{F * p * L0}{\mathrm{m}}$$

Figure SI 3. *The 2nd stress equation (X) is derived from the following quantities: σ = F/A (where stress (σ) is in Pascals, Pa, Force (F) is in Newtons, N, and Area (A) is in square meters, m^2) | ρ = m/V (where density (ρ) is in grams per cubic meter (g/m^3), mass (m) is in grams (g), and volume (V) is in cubic meters, m^3) | Ɛ = $\Delta L/L_o$ (where strain (Ɛ) is dimensionless, and both displacement (ΔL) and initial displacement (L_o) are in meters, m).*

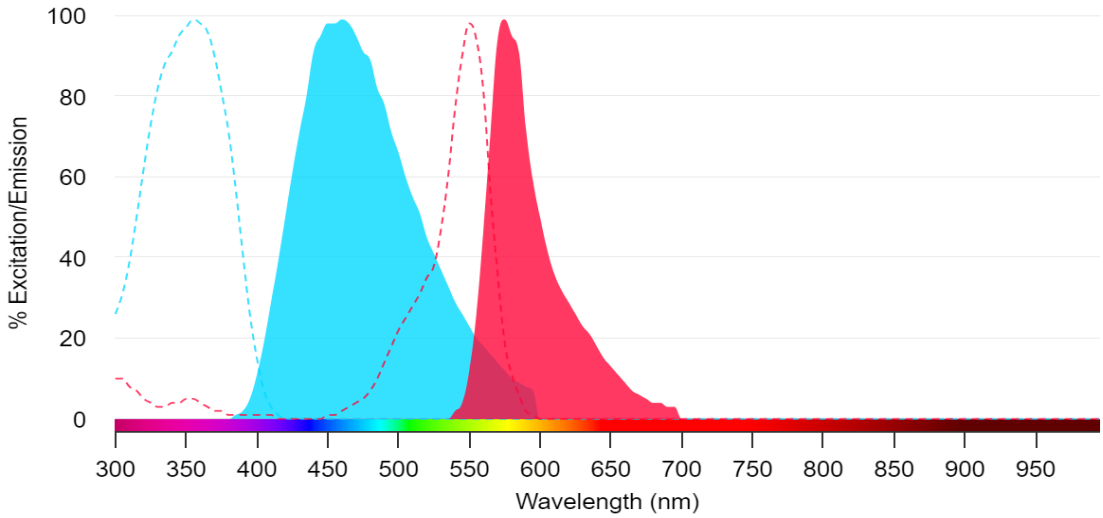

Figure SI 4. *Representation of the excitation spectra (---) and emission spectra (—) of DAPI (blue) and Phalloidin ATTO 550 (red). Image taken from FluoroFinder.*

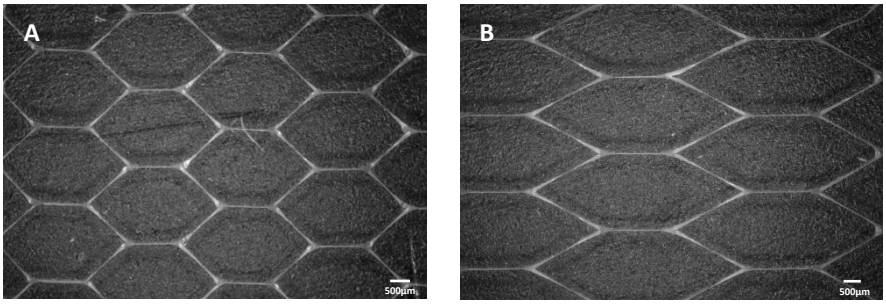

Figure SI 5. *Images acquired from top perspective by digital microscopy of two 35 layers hexagonal meshes with side length (ℓ) of 1000µm with an internal angle (θ) of 45º (A) and 30º (B). Structures were printed with the established printing parameters: P = 1 bar; z = 2.50mm; V = 4.20-4.90Kv. Images taken from VHX software*

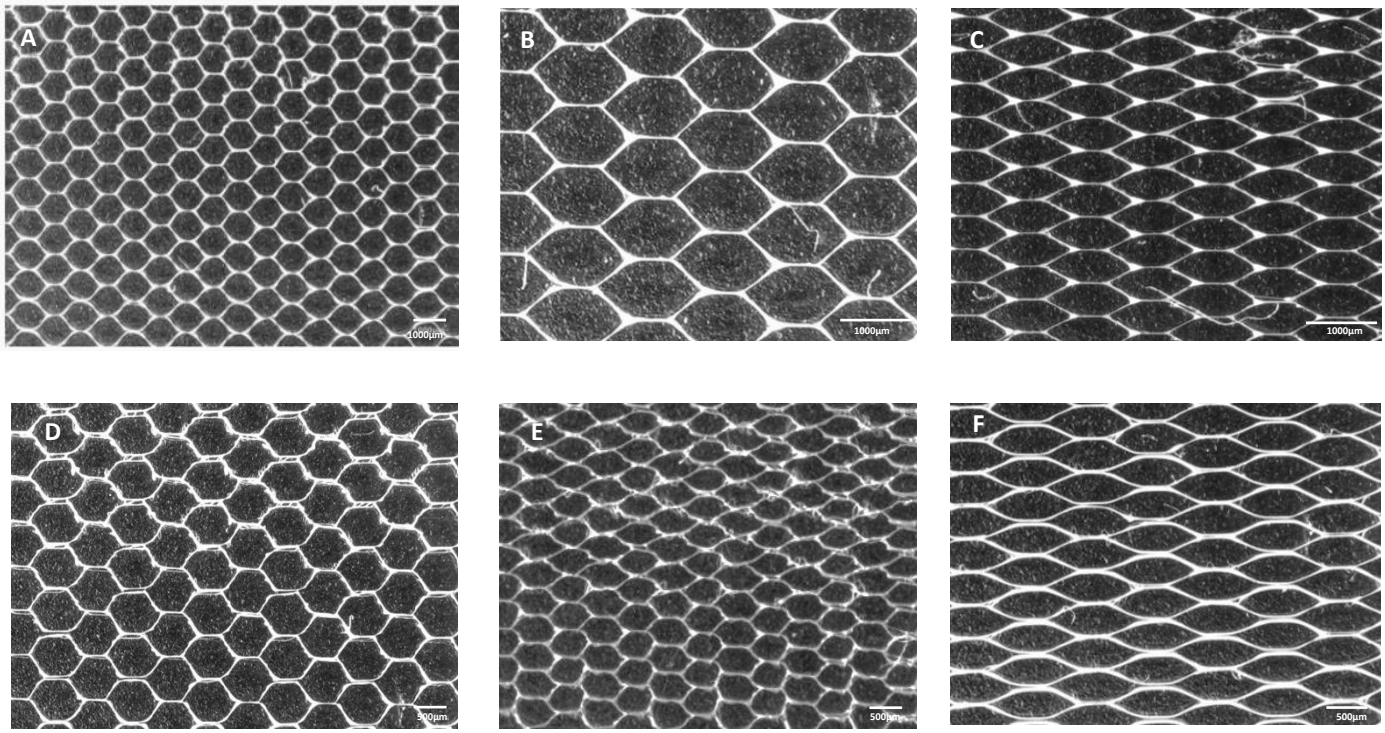

Figure SI 6. *Images acquired from top perspective by digital microscopy of two 35 layers hexagonal meshes with side length (ℓ) of 400 µm with an internal angles (θ) of 60º (A), 45º (B) and 30º (C) and 600 µm with an internal angles (θ) of 60º (D), 45º (E) and 30º (F). Structures were printed with the established printing parameters: P = 1 bar; z = 2.00mm; V = 3.70-4.00Kv. Images taken from VHX software.*

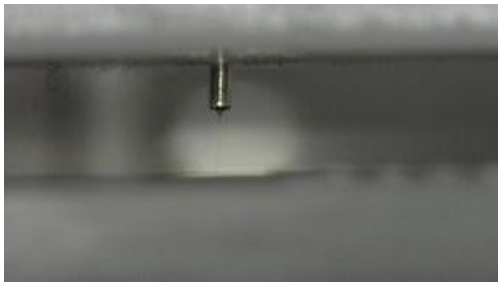

Figure SI 7. *https://vimeo.com/1010190394 Video of the jet stabilization process throughout the velocity pattern that allows the CTS to be established. Video recorded by the digital camera integrated into the MEW printer.*

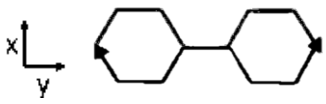

Figure SI 8. *Representative image of the print head direction during the printing of scaffolds with hexagonal structures.*

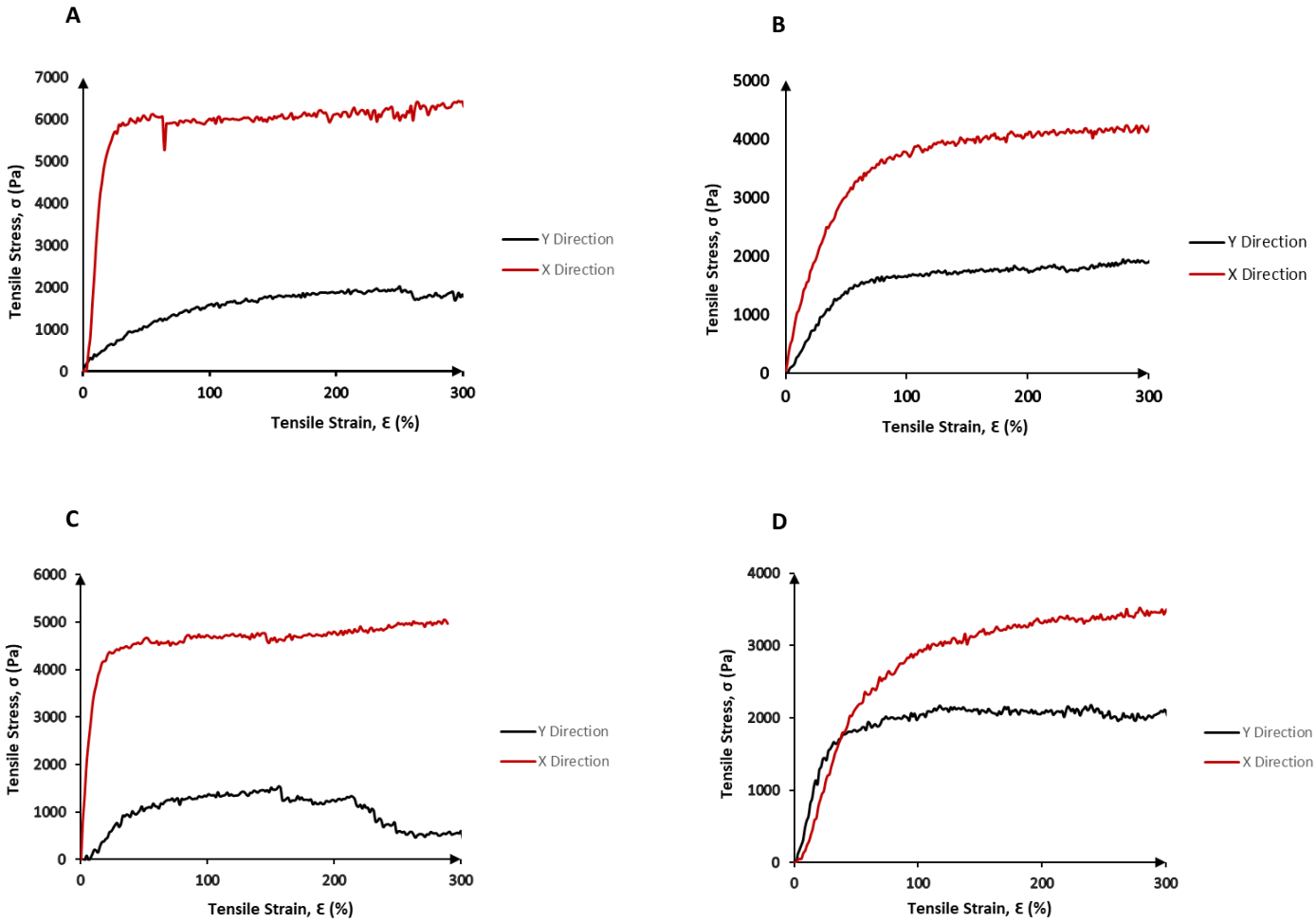

Figure SI 9. *Representation of a stress-strain curve from uniaxial tensile tests of hexagonal structures in the x-direction and y-direction, where the stress (σ) values are in Pascal (Pa) and the strain (Ɛ) values are in percentage (%) relative to the initial displacement (L0). (A) Hexagonal structure with a side length (ℓ) of 400μm with an internal angles (θ) of 30º. (B) Hexagonal structure with a side length (ℓ) of 40 0μm with an internal angles (θ) of 60º. (C) Hexagonal structure with a side length (ℓ) of 600 μm with an internal angles (θ) of 30º. (D) Hexagonal structure with a side length (ℓ) of 600μm with an internal angles (θ) of 60º.*

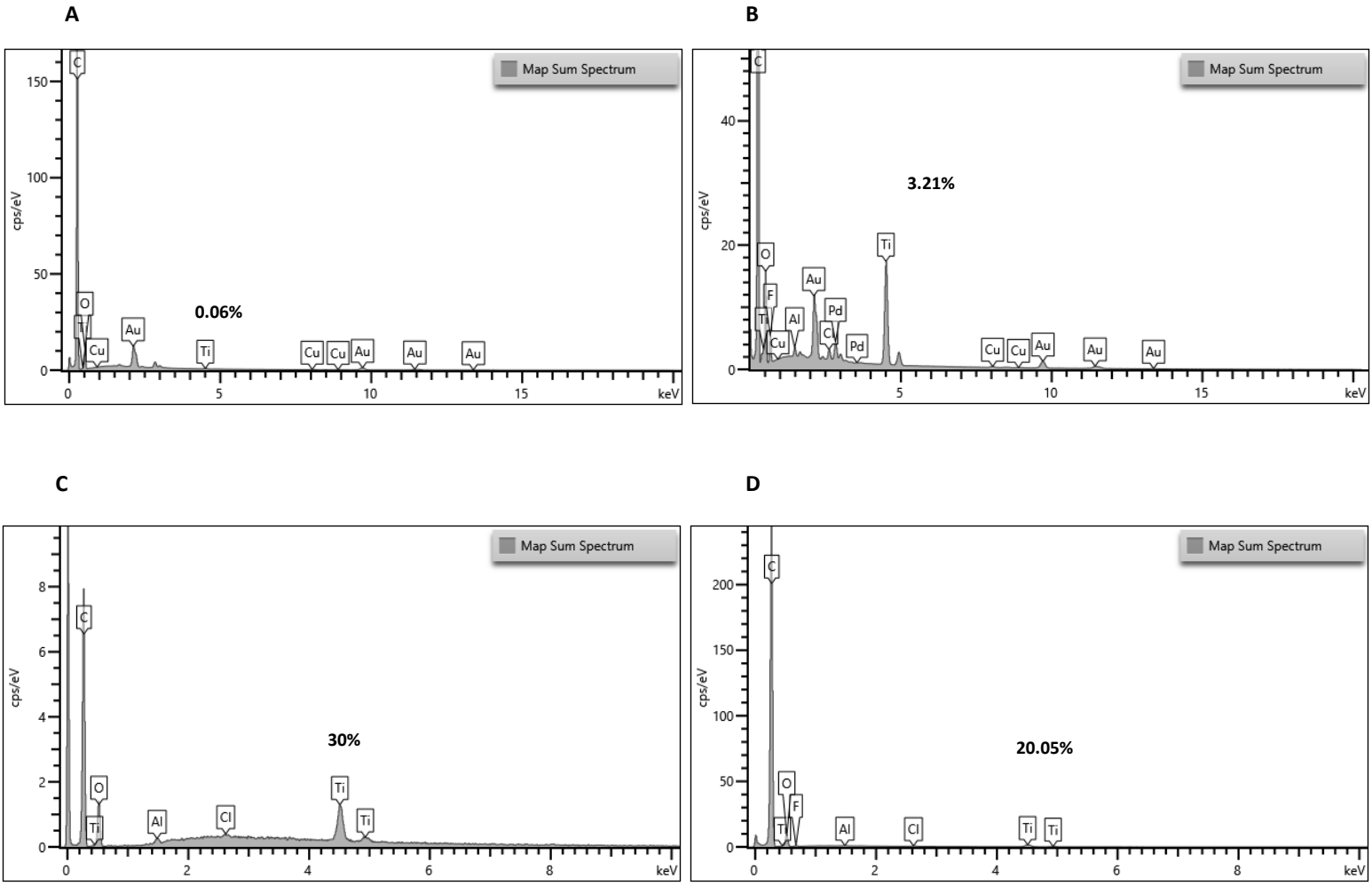

Figure SI 10. *Representation of EDS spectra with weight percent (wt%) of PCL fibers incubated with MXenes for different time periods: (A) 90 minutes, (B) 3 hours, (C) 24 hours, and with ozone treatment for 3 hours (D). On the x-axis, the energy values are in kilo-electronvolts (keV), and on the y-axis, the values are in counts per second per electron-volt (cps/eV).*